Granular Matter (2020) 22:89
https://doi.org/10.1007/s10035-020-01055-5

ORIGINAL PAPER

Evaluating the particle rolling effect on the characteristic features of granular material under the critical state soil mechanics framework

N. Barnett[1] · Md. Mizanur Rahman[1] · Md. Rajibul Karim[1] · H. B. K. Nguyen[1]

Received: 5 March 2020 / Published online: 13 October 2020

Abstract

The discrete element method (DEM) has been extensively used to capture the macroscopic and particulate response of granular materials. Although particle rolling (i.e. controlled by rolling resistance) has been acknowledged as a major contributing factor towards micro-mechanical behaviour of idealized spherical granular material, its influence on characteristic behaviour has not been thoroughly investigated within critical state soil mechanics (CSSM) framework. For instance, the influence of particle rolling on characteristic features of undrained and drained behaviour (e.g. phase transformation, characteristic state, instability, dilatancy, critical state) and the state parameter, (ψ) has not been captured. In this study, a series of constant volume (CV) and drained triaxial compression simulations were undertaken using a rolling resistance linear contact model, deployed within a DEM software. The CSSM framework was centrally used to assess the influence of particle rolling tendencies/resistance on CV and drained behaviours from both a macro- and micro-mechanical standpoint. The study advanced the current understanding of the influence of rolling resistance on CS-related behaviour.

Keywords Discrete-element modelling · Rolling resistance · Critical state soil mechanics constitutive behaviour · Fabric/structure of soils

List of symbols

Δu	Excess pore water pressure
ε_q	Deviatoric strain
ε_v	Volumetric strain
η_{IS}	Stress ratio at instability state
η_{ChS}	Stress ratio at instability state
η_{PT}	Stress ratio at phase transformation
μ	Inter-particle friction coefficient
μ_r	Rolling resistance coefficient
σ_{11}	Maximum principal stress
σ_{33}	Minor principal stress
ϕ_{cv}	Constant volume friction angle
ϕ_p	Peak friction angle
ψ	State parameter
ψ_0	State parameter at the beginning of shearing
ω_{avg}	Average angular velocity
ω_{cs}	Average angular velocity at critical state
CN	Coordination number
D_{50}	Median particle size
e	Void ratio
e_0	POST-consolidation void ratio
$\mathbf{F}$	Fabric tensor
F_{vM}	Von Mises fabric
I	Inertial number
k_n	Normal contact stiffness
k_s	Tangential contact stiffness
k_r	Rolling contact stiffness
M	Slope of CSL in $q-p'$ space
N	Total number of particles
N_c	Total number of contacts
p'	Mean effective confining stress
p'_{cs}	Mean effective confining stress at critical state

Electronic supplementary material The online version of this article (https://doi.org/10.1007/s10035-020-01055-5) contains supplementary material, which is available to authorized users.

✉ N. Barnett
nicholas.barnett@mymail.unisa.edu.au

Md. Mizanur Rahman
Mizanur.Rahman@unisa.edu.au

Md. Rajibul Karim
Rajibul.Karim@unisa.edu.au

H. B. K. Nguyen
Khoi.Nguyen@unisa.edu.au

[1] UniSA STEM, University of South Australia, Mawson Lakes, SA 5095, Australia

p'_0 Post-consolidation mean effective confining stress
q Deviatoric stress

1 Introduction

The critical state line (CSL) in e-log p' space has been used as a reference line to predict granular material behaviour; where e is the void ratio and p' is the mean effective stress. A granular material with a state (i.e. e and p') above the CSL exhibits contractive behaviour, whilst a state below the CSL exhibits dilative behaviour. Been and Jefferies [4] defined such a state with the state parameter (ψ), as the difference between current e and the e on the CSL (measured at same p') as presented in Fig. 1. In general, a positive ψ (above CSL) indicates contractive behaviour, whilst negative ψ (below CSL) indicates dilative behaviour. ψ has also been correlated with many characteristic behaviour of soil such as instability [26, 28, 59, 67, 70, 73, 74, 87], generation of excess pore water pressure (Δu) [69, 92], phase transformation (PT) and characteristic states (ChS) [55, 60, 92] and cyclic shear behaviour [69, 73, 74]. The CSL in $q-p'$ space defines intrinsic material properties such as the constant volume friction angle (ϕ_{cv}) and critical state stress ratio $M=(q/p')_{cs}$. The concept of state dependency and intrinsic material properties at CS have been used in many state-dependent constitutive models [16, 34, 42–44, 48]. Popular state-dependent constitutive models such as an earlier version of the SANISAND models described in Li and Dafalias [43] assume particle arrangement in specimens are the same i.e. formed via the same deposition/reconstitution method. However, specimens prepared by different deposition methods may have different stress–strain behaviour with same or different CSL [85] and has to be considered as different/partially different soil for constitutive modelling. The initial particle arrangement and the evolution of their interlocking, which is often indirectly captured by the mobilised inter-particle friction angle [20, 79], affects the observed stress–strain behaviour of granular materials. Therefore, understanding the evolution of particle arrangement, along with CS, is needed to develop further understanding of soil behaviour. However, capturing the micro-mechanical response of sand is challenging in an experimental setting. Experimental techniques such as Scanning Electron Microscopy (SEM) and Computed Tomography (CT) scanning have been used to capture different aspects of the micromechanical behaviour of granular materials with limited success [18, 25, 30, 89]. Although some micro-CT scanning techniques exist, which allow for the soil fabric behaviour to be captured in triaxial compression [18, 19], capturing the continuous fabric evolution behaviour using such techniques may be deemed expensive and time-consuming.

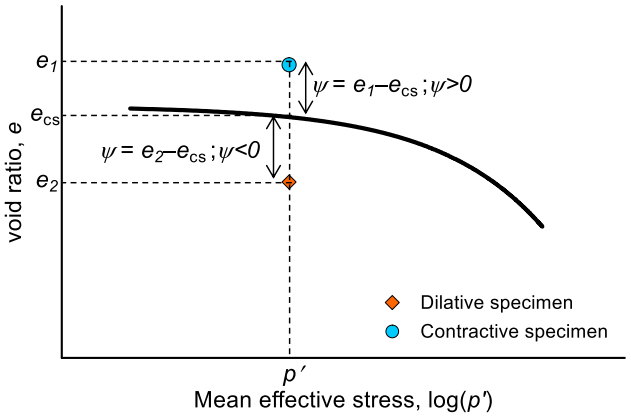

Fig. 1 Conceptualisation of the state parameter, ψ

The discrete element method (DEM), proposed by Cundall and Strack [14], has become popular as an alternative approach to develop a qualitative understanding of soil behaviour due to its capability of generating a numerical assembly of particles with a desired grain size distribution, friction coefficient and shape, and allowing an in-depth understanding of micromechanics [23, 26, 28, 59, 63]. Thus, DEM has proven to be a useful tool in capturing the micro-mechanical interactions of granular materials and is capable of providing a physical explanation of the overall behaviour of such materials. The role of fabric and contact density on the characteristic behaviour of granular materials have been explored using DEM. However, in many of these recent studies, rolling characteristics of particles have been neglected within the DEM contact model [22, 23, 93]. This is a crude assumption as many DEM studies employ spherical particles, which characteristically exhibit large particle rolling tendencies. Through X-ray and photo-elastic techniques, Oda et al. [66] and Oda and Kazama [65] suggested particle rolling is a dominant micro-deformation mechanism which controls the dilatancy and peak strength behaviours of granular materials. Their experimental study reported that rolling resistance can somewhat indirectly capture particle shape and surface texture features of granular material. Zhao et al. [95] studied the shear behaviour of variable particle shapes within a rolling resistance model in DEM and observed that particle shape could somewhat be captured by rolling resistance. However, the model was only effective in doing so for particle shapes which have slight distortion from the spherical particle. Assemblies mobilised with rolling resistance usually show higher shear strength and volumetric dilation [32, 54, 65, 94]. Liu et al. [46] reported similar observations but only until a threshold rolling resistance value of 0.3. However, Plassiard et al. [68] showed there was no clear link between rolling resistance with peak dilatancy or drained CS strength. Although, other DEM studies have observed that the addition of rolling resistance enhances the peak and

residual friction angle [1]. Iwashita and Oda [32] observed shear band formation and strain localization behaviour to intensify with the inclusion of rolling resistance, which led to higher dilative tendencies. Zhao and Guo [94] and Liu et al. [46] observed fabric anisotropy to increase with the inclusion of rolling resistance. Some studies have observed the CS to strengthen with rolling resistance, although the application of CSSM to evaluate the influence of rolling resistance on constitutional (characteristic) behaviour has not been performed [17, 100]. For example, Zhao and Guo [94] & Chang et al. [10] investigated the influence of rolling resistance within CSSM framework and observed an upwards shift of the CSL in e-log p' space with the inclusion of rolling resistance. Although, CSSM (i.e. evaluating the performance of ψ) was not used to capture the influence of particle rolling on characteristic features and constitutional shearing behaviour (e.g. phase transformation, characteristic state, undrained instability state, maximum dilatancy).

In this study, a rolling resistance linear contact model (RRLCM) is deployed in DEM to advance the understanding of the influence of particle rolling on shearing behaviour. The influence of particle rolling (or rolling resistance) on macro-mechanical features (e.g. instability, phase transformation (PT), characteristic states (ChS), peak dilatancy, CS etc.) was evaluated, advancing the understanding of the influence of particle rolling on the characteristic response of granular material. The influence of particle rolling on characteristic features was also captured via ψ (i.e. CSSM framework was utilised) and their behaviours could be bridged with the observed micro-mechanical response in the RRLCM (i.e. contact density, fabric, contact network). Currently, the ability for the CSSM (i.e. ψ) to capture the influence of particle rolling on soil behaviour is not understood. Consequently, existing state-dependent framework (e.g. the flow-rule equation in [43]) and state-dependent constitutive models and their ability to capture the influence of particle rolling on soil behaviour is not known. Through assessing the response between particle rolling resistance and the aforementioned characteristic features of triaxial compression behaviour, the ability for a state-dependent constitutive framework to capture the particle rolling effect may be analysed.

Additionally, through a focus on the DEM-observed characteristic behaviour of granular material, the understanding of the CSSM in DEM may be built upon. For instance, the recently debated [60, 92] CSSM-related phenomenon—the equivalency of the PT and ChS in undrained and drained triaxial shearing, could be analysed. Although the happening of the PT and ChS corresponds to the transition between contractive and dilative behaviours in undrained and drained triaxial shearing, the micro-mechanical influence on the happening of this transition has not been investigated. The micro-mechanical behaviour is captured at characteristic states, in order to assess the micro-mechanical influence on the happening of the PT and ChS states.

2 DEM model details

DEM software, PFC^{3D} (Itasca [31] was used to simulate constant volume (CV or undrained) and drained triaxial compression tests. Inter-particle forces and displacements were resolved using the rolling resistance linear contact model (RRLCM). The RRLCM is identical in nature to the conventional linear contact model (see Supplemental Data), however with a rolling spring and dashpot installed at the contact (Fig. 2). The rolling spring simulates the linear elastic (non-tension) frictional behaviour caused by particle rolling, whilst the dashpot accounts for any viscous behaviour due to particle rolling. It should be noted, whilst twisting may occur at the contact, the behaviour resulting from particle twisting is not incorporated in the model. Many DEM studies which attempted to analyse the influence of particle rolling behaviour have assumed constant values for either normal stiffness (k_n), tangential stiffness (k_s) and/or rolling stiffness (k_r) over an entire particle size distribution [32, 46, 54, 84]. In reality, particle stiffness has been observed to be particle size-dependent [86]. In this study, k_n, k_s and k_r of individual particles are computed based on their radius and potential deformation of particles at the contact. The deformability of granular material which share contact can be described by the elastic constants of the material, i.e. Young's modulus (E) and Poisson's ratio (ν). In this study, k_n, k_s and k_r are a direct function of an effective modulus (E^*) and $k^* = k_n/k_s$, which are emergent properties of E and ν. The method of deformability installed in the contact model and the mathematical formulations of k_n, k_s and k_r are further described in Appendix A. An average contact overlap ratio representative of sand particles was maintained. That is, an average overlap ratio less than 6% was achieved [51]. An $E^* = 50$ MPa was selected and critical state stress ranges (i.e. p'_{cs}) observed in this study aligned with those observed in experimental studies of identical graded granular material [75]. Unlike other studies, this study therefore evaluates the rolling behaviour of particles where contact stiffness varied with radius and potential deformation. The full mathematical description of the inherited RRLCM is presented in "Appendix B".

Various approaches have been used to mimic the rolling resistance (or potential) created at a contact. Two of the more common methods of modelling rolling resistance in DEM is through either- 1) an eccentricity parameter [98, 99] with a unit length which is related to a rolling moment arm between two contacting particles or 2) a dimensionless shape parameter, δ [35] which apparently reflected the contact width between contacting entities and their relative particle shapes. A more commonly used approach is adopting

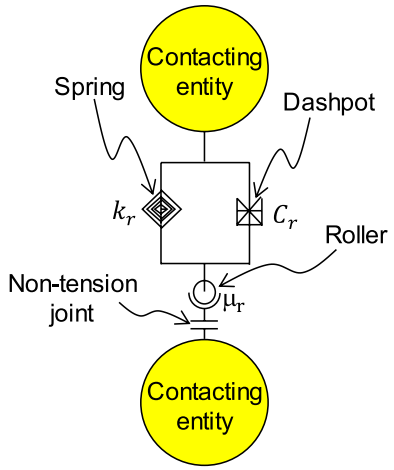

Fig. 2 Rheology of rolling contact mechanism used in study

a dimensionless rolling resistance parameter (μ_r) due to its established physical basis:

$$\mu_r = \tan\beta \tag{1}$$

where β corresponds to the maximum angle of a plane at which a particle sitting on it possesses a resisting moment equal to its natural rolling torque. The mathematical definition of μ_r is conveniently in close association with the definition of angle of repose and therefore sliding friction (μ). Further, Ai et al. [2] indicated that the μ_r definition is preferable in measuring rolling resistance due to its clear physical basis. μ and μ_r were used simultaneously in all simulations. In this study, various μ_r values were used to investigate the effect of particle rolling on overall behaviour.

3 Triaxial simulations

In this study, 90 triaxial tests with different consolidation stresses, p'_0 (48–500 kPa), different initial void ratio, e_0 (0.594–0.889) and different μ_r (0–1) were simulated. A summary of DEM input parameters and test conditions are presented in Tables 1 and 2 respectively. The range of $0 \le \mu_r \le 1$ was selected as at $\mu_r \approx 1$ a threshold rolling value is approached, and minimal change in soil and CS behaviour were observed.

Spherical particles were used to represent clean sand with median particle size, D_{50} of 0.279 mm. The particle size distribution of the assembly is presented in Fig. 3. Particles were initially generated with no initial contact within a cubic domain bounded by six rigid and frictionless walls. A staged isotropic compression technique was used to achieve the desired void ratio before consolidation, e_i. During this process, a smaller μ ($\approx$0–0.4) was used to form dense assemblies, whilst a large μ ($\approx$0.6–1) was used to form loose assemblies. After the desired e_i was achieved, μ was set to a representative value for granular material ($\mu = 0.5$) before the commencement of consolidation in all triaxial simulations. All specimens were isotropically compressed to different p'_0.

Table 1 Summary of the specimen testing in DEM

Parameter	Value
Particle density (ρ_g)	2650 kg/m^3
Effective Young's modulus (E^*)	50 MPa
Inter-particle sliding friction coefficient (μ)	0.5
Wall friction coefficient	0
Wall stiffness	1×10^{10} kN/m
Damping constant	0.7

In undrained (constant volume) shearing constant volume was ensured through a servo-control mechanism applied to the vertical walls while shearing strains were applied at the top and bottom walls. Drained shearing was achieved through strain control of the top and bottom walls, whilst the stresses on the vertical walls were controlled simulating constant cell pressure.

4 Numerical stability of DEM simulations

The deterministic nature of elastoplastic theories suggests that the mechanical behaviour of granular material in DEM assemblies should be independent of size i.e. number of particles [36]. Figure 4 presents the shearing responses for three specimens with different particle number (N) and strain deformation rates. TRR26 and TRR31 were conducted with the same strain rate of strain of 0.001 s^{-1} but with $N = 10{,}506$ and $N = 17{,}921$ respectively. TRR33 was conducted with $N = 10{,}506$ and a strain rate five times smaller than TRR26 (0.0002 s^{-1}). Negligible discrepancies in their q–ε_q and q–p' paths in Fig. 4a, b suggest that a strain rate of 0.001 s^{-1} with $N = 10{,}506$ achieves numerical stability. This specimen size and strain rate was used in all further simulations in this study.

The coordination number, $CN = 2N_c/N$ [78], is a micromechanical entity which quantifies the contact density of a granular assembly; where N_c is the number of particle contacts. Figure 4c shows that specimen size and strain rate had a negligible influence in their CN-ε_q paths. The inertial number (I) proposed by da Cruz et al. [15] has been used as a performance parameter in DEM which assesses whether a quasi-static deformation of particles in the assembly throughout shearing is upheld. I is defined as,

$$I = \dot{\varepsilon} d \left(\rho_g / p\right)^{0.5} \tag{2}$$

Table 2 Summary of DEM simulations

Test ID	μ_r	p'_0 (kPa)	e_0	p'_{cs} (kPa)	CN_{cs}	ψ_0
T1	0.30	96	0.867	0.3	--	0.017
T2	0.30	96	0.597	1298.0	--	−0.253
T3	0.30	96	0.838	138.4	--	−0.012
T4	0.30	96	0.667	931.3	--	−0.183
T5	0.30	96	0.726	652.9	--	−0.124
T6	0.30	96	0.852	23.9	--	0.002
T7	0.30	96	0.796	337.7	--	−0.054
T10	0.30	96	0.675	845.9	4.41	−0.175
T11	0.30	333	0.547	1529.0	5.08	−0.248
T12	0.30	96	0.726	625.9	4.08	−0.124
T13	0.30	96	0.875	0.1	1.79	0.025
T14	0.30	96	0.796	353.8	3.73	−0.054
T15	0.30	500	0.746	572.6	4.00	−0.013
T16	0.30	500	0.742	580.3	4.05	−0.017
T17	0.30	500	0.722	629.4	4.13	−0.037
T18	0.30	96	0.597	1285.9	4.83	−0.25
T-RR1	0.00	96	0.594	886.1	5.25	−0.116
T-RR2	0.50	96	0.599	1280.000	4.76	−0.274
T-RR3	0.70	96	0.599	1313.0	4.69	−0.274
T-RR4	0.30	96	0.599	1231.0	4.79	−0.251
T-RR5	0.30	96	0.874	0.2	1.83	0.024
T-RR7	0.00	96	0.718	35.5	3.82	0.008
T-RR8	0.50	100	0.885	0.3	1.74	0.013
T-RR9	0.50	450	0.657	1042.0	4.47	−0.141
T-RR10	0.00	350	0.670	363.3	4.65	−0.002
T-RR11	0.00	350	0.671	374.2	4.67	−0.001
T-RR12	0.70	100	0.668	969.3	4.39	−0.204
T-RR13	0.70	100	0.864	190.4	2.98	−0.008
T-RR14	0.70	350	0.788	481.9	3.69	−0.032
T-RR15	0.70	350	0.627	1176.9	4.56	−0.193
T-RR16	0.70	100	0.889	13.4	2.04	0.017
T-RR17	0.00	100	0.670	396.7	4.69	−0.039
T-RR21	0.02	100	0.601	917.9	5.19	–
T-RR22	0.00	100	0.594	886.0	5.25	−0.116
T-RR24	0.10	100	0.600	1068.8	4.98	−0.185
T-RR25	0.20	100	0.601	1189.9	4.88	–
T-RR26	0.30	100	0.599	1304.0	4.85	−0.25
T-RR28	0.60	100	0.597	1292.0	4.73	–
T-RR29	0.80	100	0.601	1273.9	4.68	–
T-RR30	1.00	100	0.598	1344.0	4.71	–
T-RR31	0.30	100	0.589	1282.0	4.89	−0.260
T-RR33	0.30	100	0.596	1244.0	4.78	−0.253
T-RR34	0.10	100	0.601	1088.9	5.01	−0.184
T-RR35	0.10	100	0.741	337.2	4.11	−0.044
T-RR36	0.10	100	0.793	0.7	2.76	0.007
T-RR37	0.10	350	0.730	398.3	4.21	−0.011
T-RR38	0.10	350	0.742	313.7	4.07	0.000
T-RR39	0.10	100	0.807	0.4	2.63	0.022
T-RR40	0.10	100	0.802	0.3	2.63	0.017
T-RR41	0.10	100	0.794	0.7	2.82	0.009
T-RR42	0.10	100	0.793	0.6	2.76	0.008

Table 2 (continued)

Test ID	μ_r	p'_0 (kPa)	e_0	p'_{cs} (kPa)	CN_{cs}	ψ_0
T-RR43	0.10	200	0.767	227.6	3.92	−0.001
T-RR46	0.00	100	0.719	8.8	3.52	0.009
T-RR47	0.00	100	0.717	5.1	3.48	0.007
T-RR48	0.00	48	0.731	0.6	3.06	0.013
T-RR49	0.00	76	0.723	1.4	3.22	0.009
T-RR50	0.00	100	0.720	9.8	3.55	0.010
T-RR51	0.10	100	0.765	210.1	3.88	−0.020
T-RR52	0.10	100	0.790	104.7	3.57	0.005
T-RR53	0.10	76	0.798	0.6	2.79	0.008
T-RR54	0.30	76	0.853	4.6	2.33	−0.002
T-RR55	0.30	100	0.859	89.9	2.97	0.010
T-RR56	0.50	120	0.849	206.8	3.15	−0.019
T-RR57	0.50	50	0.878	102.6	2.78	−0.004
T-RR59	0.50	120	0.876	155.9	2.98	0.008
T-RR60	0.70	80	0.861	204.8	3.07	−0.015
T-RR-D1	0.00	96	0.594	129.1	4.22	−0.116
T-RR-D2	0.50	96	0.599	174.3	3.03	−0.274
T-RR-D3	0.70	96	0.599	188.2	3.00	−0.008
T-RR-D4	0.30	96	0.597	157.7	3.20	−0.253
T-RR-D6	0.00	350	0.666	474.6	4.83	−0.006
T-RR-D7	0.00	450	0.628	600.9	4.96	−0.030
T-RR-D8	0.00	200	0.699	268.3	4.52	0.005
T-RR-D9	0.00	100	0.723	131.4	4.14	0.013
T-RR-D10	0.00	100	0.724	132.4	4.15	0.014
T-RR-D11	0.50	100	0.728	176.9	3.04	−0.144
T-RR-D12	0.50	100	0.853	185.9	3.01	−0.019
T-RR-D13	0.50	100	0.881	178.2	3.01	0.009
T-RR-D14	0.50	100	0.874	185.2	3.05	0.002
T-RR-D15	0.50	350	0.726	614.3	3.92	−0.094
T-RR-D16	0.50	450	0.614	808.7	4.23	−0.184
T-RR-D17	0.50	350	0.800	622.0	3.95	−0.020
T-RR-D18	0.50	100	0.884	180.1	2.99	0.012
T-RR-D19	0.50	350	0.792	632.0	3.95	−0.028
T-RR-D20	0.30	350	0.744	580.9	4.06	−0.047
T-RR-D21	0.30	100	0.836	169.5	3.21	−0.013
T-RR-D22	0.30	350	0.675	575.6	4.05	−0.116
T-RR-D23	0.30	100	0.866	168.8	3.20	0.017
T-RR-D24	0.30	450	0.754	755.7	4.26	−0.016
T-RR-D25	0.70	450	0.660	836.6	4.19	−0.032
T-RR-D26	0.70	100	0.875	193.5	3.04	−0.193
T-RR-D27	0.70	100	0.849	196.0	2.99	0.017
T-RR-D28	0.70	350	0.772	679.2	3.96	−0.015
T-RR-D30	0.02	100	0.601	138.5	4.13	–
T-RR-D33	0.20	100	0.601	156.5	3.42	–
T-RR-D39	0.10	100	0.741	147.8	3.73	−0.044
T-RR-D40	0.10	350	0.730	511.4	4.39	−0.012
T-RR-D41	0.10	350	0.737	509.3	4.38	−0.005
T-RR-D42	0.10	96	0.601	139.6	3.71	−0.185
TRR-D44	0.10	300	0.672	438.8	4.26	−0.079

"–" Denotes no CSL was constructed for μ_r value. Hence no ψ_0 value is reported

"--" Denotes micromechanics were not measured for simulation

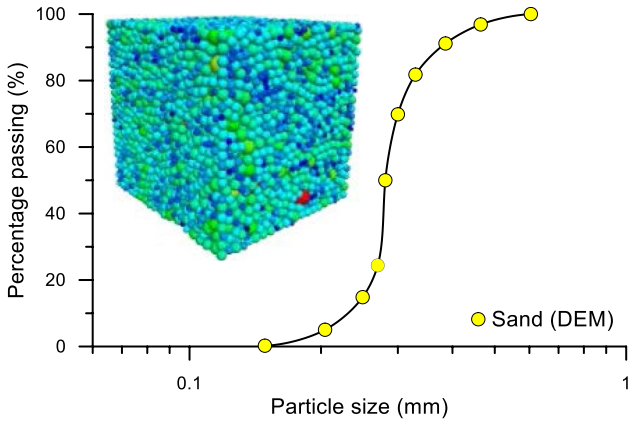

Fig. 3 DEM assembly and its particle size distribution

where $\dot{\epsilon}$ is the shear strain rate, d is the mean particle diameter, and ρ_g is the particle density. All simulations satisfied the condition of $I < 10^{-3}$ i.e. the influence of particle kinematics on the observed shear behaviour corresponded to a quasi-static condition [47, 50].

5 Results

The major and minor principal stresses (σ'_{11} and σ'_{33}) were computed from the stress tensor as suggested by Christoffersen et al. [11]:

$$\sigma'_{ij} = \frac{1}{V} \sum_{c \epsilon N_c} f_i^c l_j^c \tag{3}$$

where V is the total assembly volume, N_c is the total number of contacts, f_i^c is the ith component of contact force at contact c and l_j^c represents the jth branch vector connecting the centres of two contacting particles, at contact c. Only particle to particle contacts are considered in Eq. 3 so that the effect of the rigid boundary end-restraint is reduced [21, 49]. p' and q (in triaxial space) were derived from the stress tensor as below:

$$p' = \frac{\sigma'_{11} + \sigma'_{33}}{3} \tag{4}$$

$$q = \sigma'_{11} - \sigma'_{33} \tag{5}$$

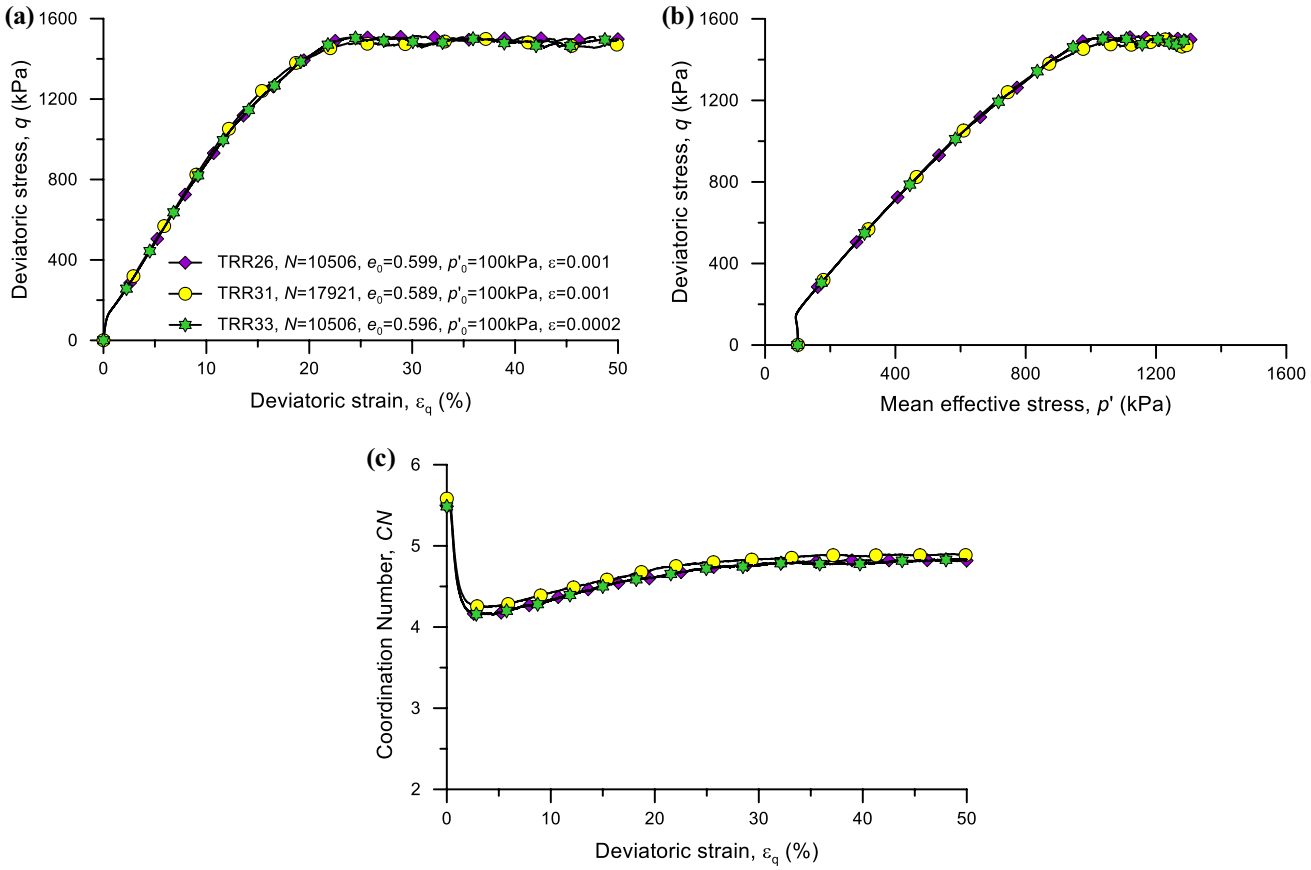

Fig. 4 Effect of specimen size and strain rate on DEM simulation in: **a** $q - \varepsilon_q$, **b** $q - p'$ and **c** $CN - \varepsilon_q$ spaces

5.1 Constant volume tests

Figure 5 shows the response during CV shearing for six samples with different μ_r ($0 \leq \mu_r \leq 1$). All tests were conducted with p'_0 of 100 kPa and similar e_0 values (between 0.594 and 0.601). Each simulation was continued up to ε_q of 50%. Due to the very dense nature of the presented tests, a strict condition of CS was sometimes not reached, as the condition $d\Delta u = 0$ was not satisfied. Note, Δu was indirectly derived from the difference between p' in CV and drained paths ($\Delta u = p'_D - p'_{CV}$) as described by Sitharam et al. [81]. In cases where the CS condition of $d\Delta u = 0$ was not reached, an extrapolation approach [8, 55, 75] was used. All specimens underwent strain hardening until a near CS was reached, and therefore exhibited non-flow (NF) behaviour. Specimens with large μ_r values manifested the strongest behaviour characterised by prolonged strain hardening legs, resulting in the manifestation of larger CS strengths. An identical trend reoccurred in effective stress path space (Fig. 5b), suggesting the increase in strength with μ_r is largely due to the enhancement of frictional properties. In Fig. 5a, b, $M = q/p'$ or CS strength increased with μ_r, but became less sensitive to changes as $\mu_r \rightarrow 1$ indicating a theoretical state of maximum rolling resistance is approached. The DEM study of Huang et al. [26, 28] detected similar behaviour in the case of μ.

The influence of μ_r on Δu is evaluated in Fig. 5c. When $\varepsilon_q < 25\%$, assemblies mobilised with low μ_r were observed to exhibit the largest negative pore water pressure changes. Although, assemblies with larger μ_r, generate negative Δu at larger rates past intermediate ($\approx 25\%$,) strains. A clear trend between Δu and μ_r at CS is hard to observe as most tests are yet to reach CS and are changing at different rates.

Earlier studies suggested that a large *CN* is often associated with a large CS strength or dense assembly [22, 59]. To evaluate the effect of μ_r on *CN*, the isotropic compression paths are presented first in Fig. 6a. A negligible influence of μ_r on *CN* was observed, i.e. these paths were almost identical. The evolution of *CN* during shearing was then presented in Fig. 6b. Although *CN* at the start of shearing is identical for all simulations, during shearing, a specimen with larger μ_r value achieved a lower *CN* at the critical state and vice versa. For instance, assemblies with large rolling tendencies (lower μ_r) achieved a critical state strength via a larger number of weaker contacts. On the other hand, the efficiency of strong contact formation was superior for assemblies mobilised with a larger μ_r. The strong formation efficiency or interlocking behaviour may therefore be tuned via μ_r.

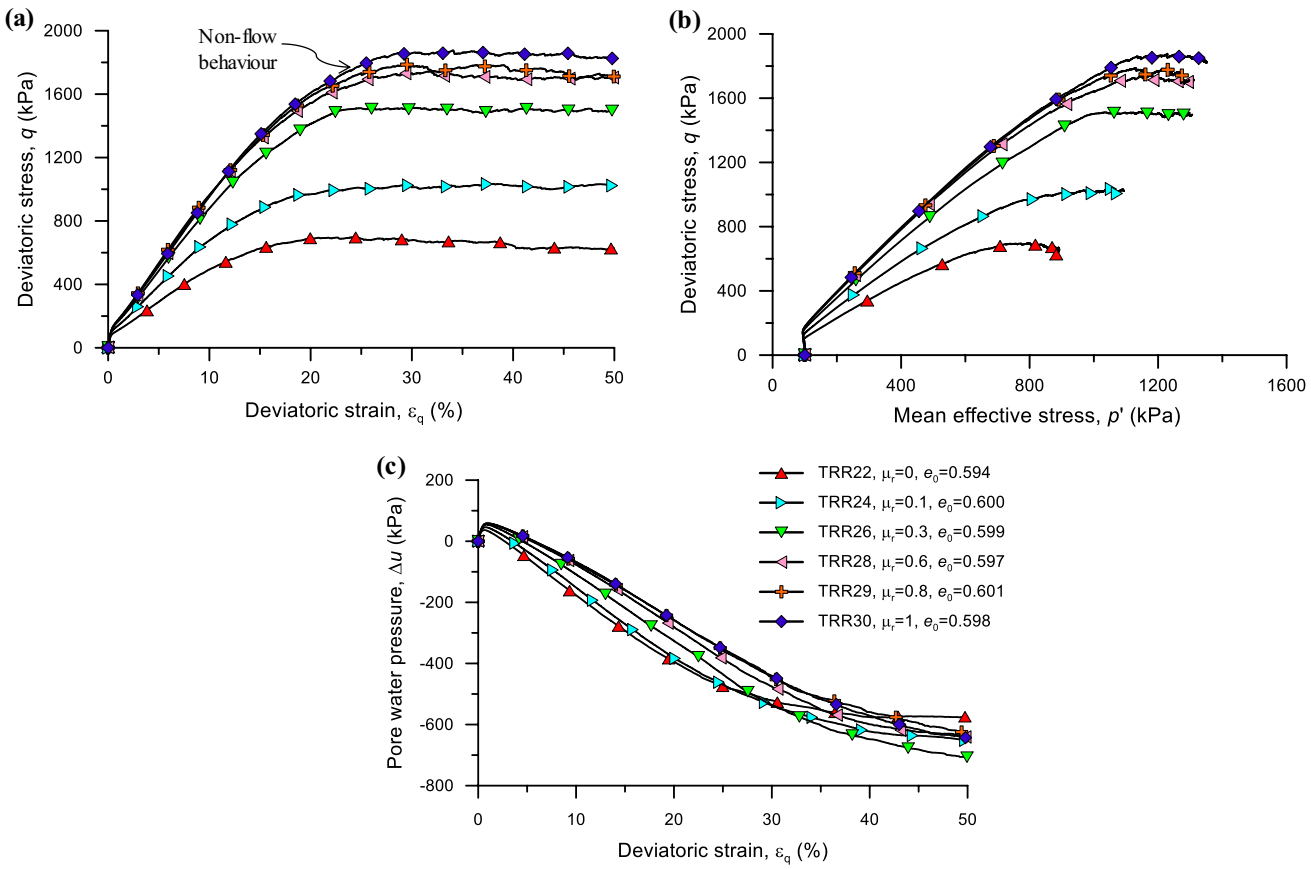

Fig. 5 Influence of μ_r on CV behaviour in **a** $q - \varepsilon_q$, **b** $q - p'$ and **c** $\Delta u - \varepsilon_q$ spaces

Although, these findings are important in understanding the qualitative influence of particle rolling on contact density, the RRLCM may have the tendency to generate magnitudes of *CN* which may not be realistic [95].

The contact force networks at CS for four undrained specimens with similar initial states but varying μ_r illustrate this effect (Fig. 7). A profound influence of particle rolling on the contact force network and the contact anisotropy throughout shearing can be observed. In a free-rolling environment (i.e. $\mu_r = 0$, Fig. 7a) a dense contact network was formed (i.e. large *CN*). The network was rife with contacts largely disorientated to the direction of loading, i.e. weak contact forces were predominate [52]. Following Radjai et al. [72], an assembly which possesses a contact network of this type may behave as an interstitial fluid. In agreement, Zhou et al. [97] indicated the reduction in μ_r conforms to a lubrication or softening effect of particles in contact. When μ_r was large, strong contacts with larger magnitude (i.e. a hardening effect) dominated the force chain network, ultimately with a reduction of *CN* at CS. The amount of sliding or rolling contacts are therefore limited [72] and ultimately interlocking capabilities are enhanced. Guo and Su [24] in their laboratory experiments and Huang et al. [26, 28] in their DEM simulations also observed interlocking behaviour to be closely related with particle angularity—a parallel that could be drawn between particle rolling resistance and angularity. Although an interlocking effect can be simulated via rolling resistance, through capturing the twisting resistance at the contact, the interlocking could be better approximated.

The change in force chain networks could also be explained by a transitional behaviour from rolling-dominanting contact networks to sliding-dominating contacts networks, as μ_r is varied. Reportedlty, for the granular mixtures mobilised with small μ_r values, the displacement of contacts are dominated by particle rolling. As μ_r increased, the participation of sliding at the contacts was increased, in lieu of rolling behaviour [27]. Nevertheless, a clear strengthening effect is observed with the addition of μ_r.

Many studies have reported the internal structure or spatial arrangement (i.e. soil fabric) of granular material to be highly anisotropic which influences the soil behaviour [56, 64, 91]. Similar to *CN*, observing the anisotropic fabric and its evolution throughout shearing may assist in explaining the macro-response of a granular material. To quantify anisotropic fabric, Satake [80] and Rothenburg and Bathurst [78] proposed similar second-order fabric tensors. Via the former, the fabric tensor, **F** may be expressed as:

$$\mathbf{F} = F_{ij} = \frac{1}{N_c}\sum_{k=1}^{N_c} n_i^k n_j^k = \begin{pmatrix} F_{11} & F_{12} & F_{13} \\ F_{21} & F_{22} & F_{23} \\ F_{31} & F_{32} & F_{33} \end{pmatrix} \tag{6}$$

where n^k is the directional unit vector for the kth contact, F_{ij} is scalar counterpart of **F**. Rahman et al. [76] showed that the deviatoric fabric and its evolution throughout shearing could be represented by the von Mises fabric, $F_{vM} = 3(F_{J2D})^{0.5}$[77], where F_{J2D} represents the second invariant of **F**:

$$F_{J2D} = \frac{1}{6}\left[\left(F_{11}-F_{22}\right)^2 + \left(F_{11}-F_{33}\right)^2 + \left(F_{22}-F_{33}\right)^2\right] + F_{12}^2 + F_{13}^2 + F_{23}^2 \tag{7}$$

Figure 8 illustrates the evolution of deviatoric fabric for each of the CV simulations. The deviatoric fabric intensified to a peak F_{vM} and then reduced until CS was reached where the changes of von Mises fabric dF_{vM} approached zero. In agreement with Li and Dafalias [41], $dF_{vM} = 0$ may be considered as a supplementary condition of CS. Specimens mobilised with large μ_r values displayed a large peak and CS F_{vM}. Assemblies with large strong contact networks

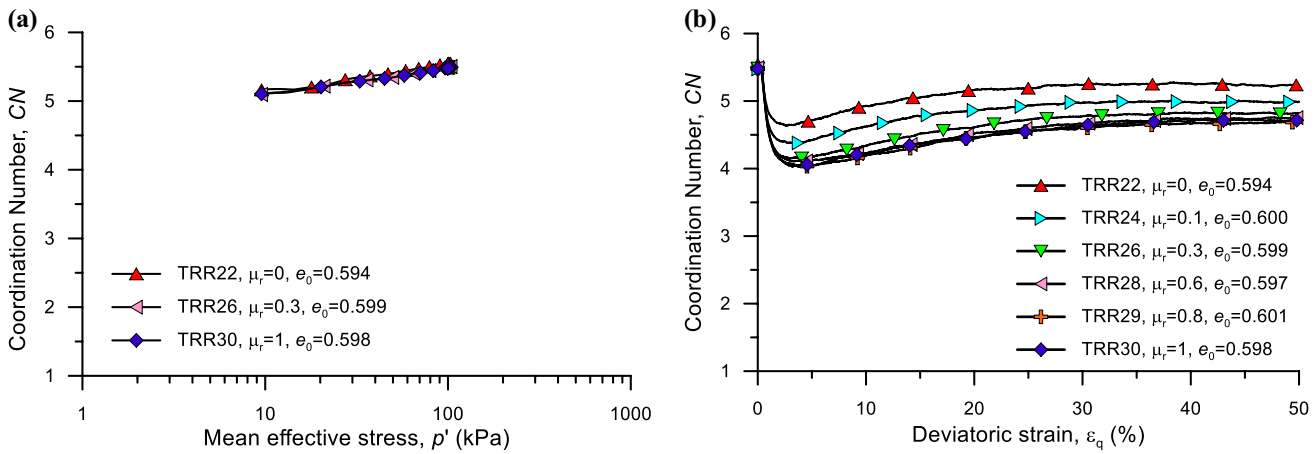

Fig. 6 Influence of μ_r on **a** isotropic consolidation behaviour in $CN - p'$ space, **b** CV shear behaviour in $CN - \varepsilon_q$ space

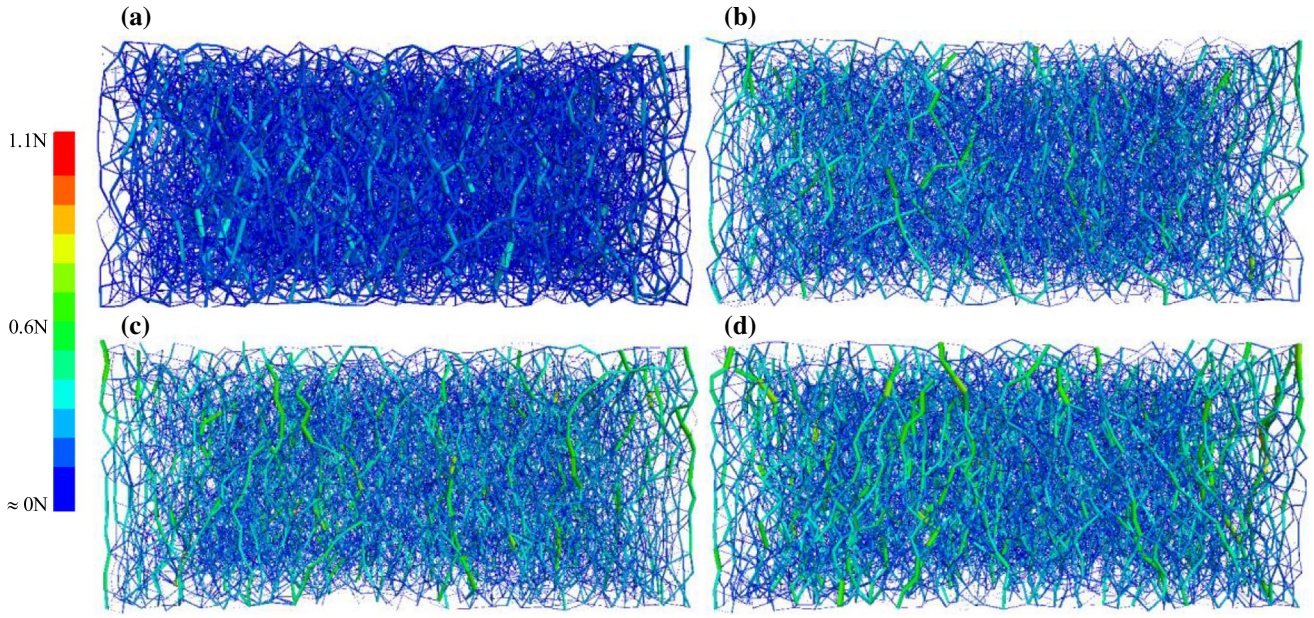

Fig. 7 Influence of rolling resistance on observed contact network at CS: **a** TRR22 ($\mu_r = 0$), **b** TRR25 ($\mu_r = 0.2$), **c** TRR28 ($\mu_r = 0.6$), **d** TRR30 ($\mu_r = 1.0$)

typically exhibit large anisotropy [26, 28], which potentially explains why assemblies with large μ_r exhibit large peak F_{vM} or deviatoric anisotropies. The observations also highlight that the deviatoric fabric is largest for assemblies mobilised with large μ_r [96].

The phase transformation (PT) state corresponds to the transition from contractive to dilative behaviour, which may be observed in the undrained shearing of dense and medium-dense specimens. Mathematically the PT can be defined as when $dp' = 0$ [38] and corresponds to the 'knee' in the effective stress path as shown in Fig. 9a. Alternatively, $d\Delta u = 0$ has been used to define the PT state as shown in Fig. 9b [83]. The later description ($d\Delta u/d\varepsilon_q = 0$) was used to define PT in this study. The rolling tendencies manifested within an assembly was observed to influence the PT. Specifically, the PT was observed at slightly larger ε_q, Δu and q values for assemblies with larger μ_r. In Fig. 9c the PT point observed at $d\Delta u = 0$ was projected on the *CN* evolution path for each simulation. Interestingly, the PT point does not correspond to a change in contact behaviour, i.e. a change from decreasing contact density to increasing contact density. Literature has linked the local minimum of the *CN* path to the quasi-steady state [88], although it seems there is no relation with the classical PT point. The PT point was also projected on the fabric evolution path (Fig. 9d). It seems, the occurrence of PT cannot be explained by a sudden change (local maximum) in the granular material deviatoric fabric or spatial arrangement. The *CN* and F_{vM} behaviour has been useful in explaining CS behaviour from a micromechanical standpoint [3, 26, 28, 57], although explaining the occurrence of PT from these two micromechanical entities is challenging.

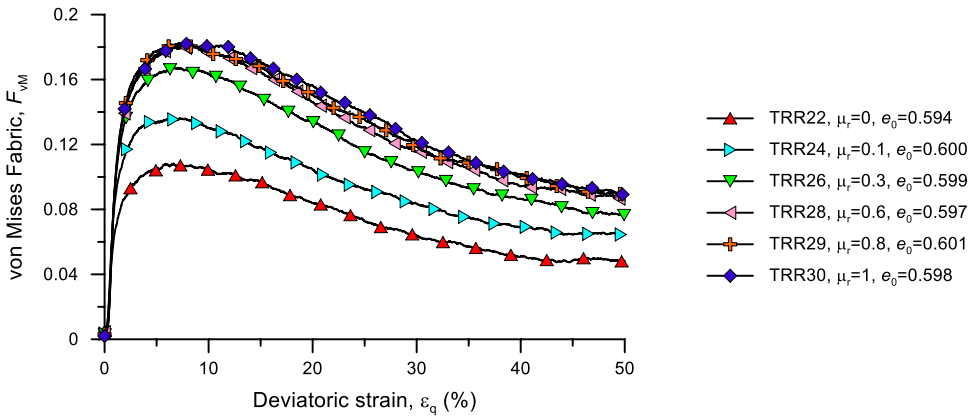

Fig. 8 Influence of μ_r on CV behaviour in $F_{vM} - \varepsilon_q$ space

At the happening of PT a sharp change from contractive to dilative behaviour is observed. Although, such behaviour is not believed to arise as a result of DEM imposed testing conditions. For instance in Ishihara [29] study of Toyoura sand, a sharp change from contractive to dilative behaviour was also observed. In the experimental study of Murthy et al. [55] a clear 'knee' in the effective stress path could also be observed—both studies yielded similar 'knee' or PT behaviour as this manuscript.

5.2 Drained shearing tests

Figure 10 shows the drained shearing responses for samples with p'_0 of 100 kPa, e_0 within a narrow range of 0.594–0.601 and varying of μ_r values. In Fig. 10a, all specimens exhibited dilative behaviour to a peak deviatoric stress (q_{peak}) followed by strain-softening to CS. Similar to the observations made for constant volume shearing, an increase in CS strength is associated with a rise in μ_r (see Fig. 10a). For large μ_r, hardening occurred over a larger range of ε_q, thus a higher q_{peak} was reached at larger deviatoric strains. Specimens with large μ_r manifested steep strain softening (i.e. brittle) behaviour.

The highly dilative nature of assemblies mobilised with large μ_r is illustrated in $\varepsilon_v - \varepsilon_q$ space; where ε_v represents the volumetric strain (Fig. 10b). Volume dilation shows to increase with μ_r. Although, when $\mu_r > 0.3$, insignificant increase in volume dilation occurs. Each of the drained tests peak dilatancy, i.e. $d_{peak} = \left(\frac{d\varepsilon_q^p}{d\varepsilon_v^p}\right)_{peak}$, was captured (Fig. 10c); where superscript "^{p}" refers to plastic. Note, following many researchers $d\varepsilon_q^p \approx d\varepsilon_q$ and $d\varepsilon_v^p \approx d\varepsilon_v$ were assumed for large strain behaviour of granular materials [43, 73, 74]. Figure 10c supports the supposition that there is insignificant change in dilatancy behaviour at ranges of $\mu_r > 0.3$ is further supported. Although in $q - \varepsilon_q$ space at $\mu_r > 0.3$, the change in peak strength is more significant. Thus, at this range of μ_r it seems an enhancement of frictional properties (i.e. M or ϕ_{cv}) rather than dilatancy properties is responsible for strengthening the materials response via strong contacts. When $\mu_r < 0.3$, the response is governed more equally by both dilatancy as well as frictional behaviour. In Fig. 10c, the peak dilatancy, was observed to increase initially with μ_r although Plassiard et al.

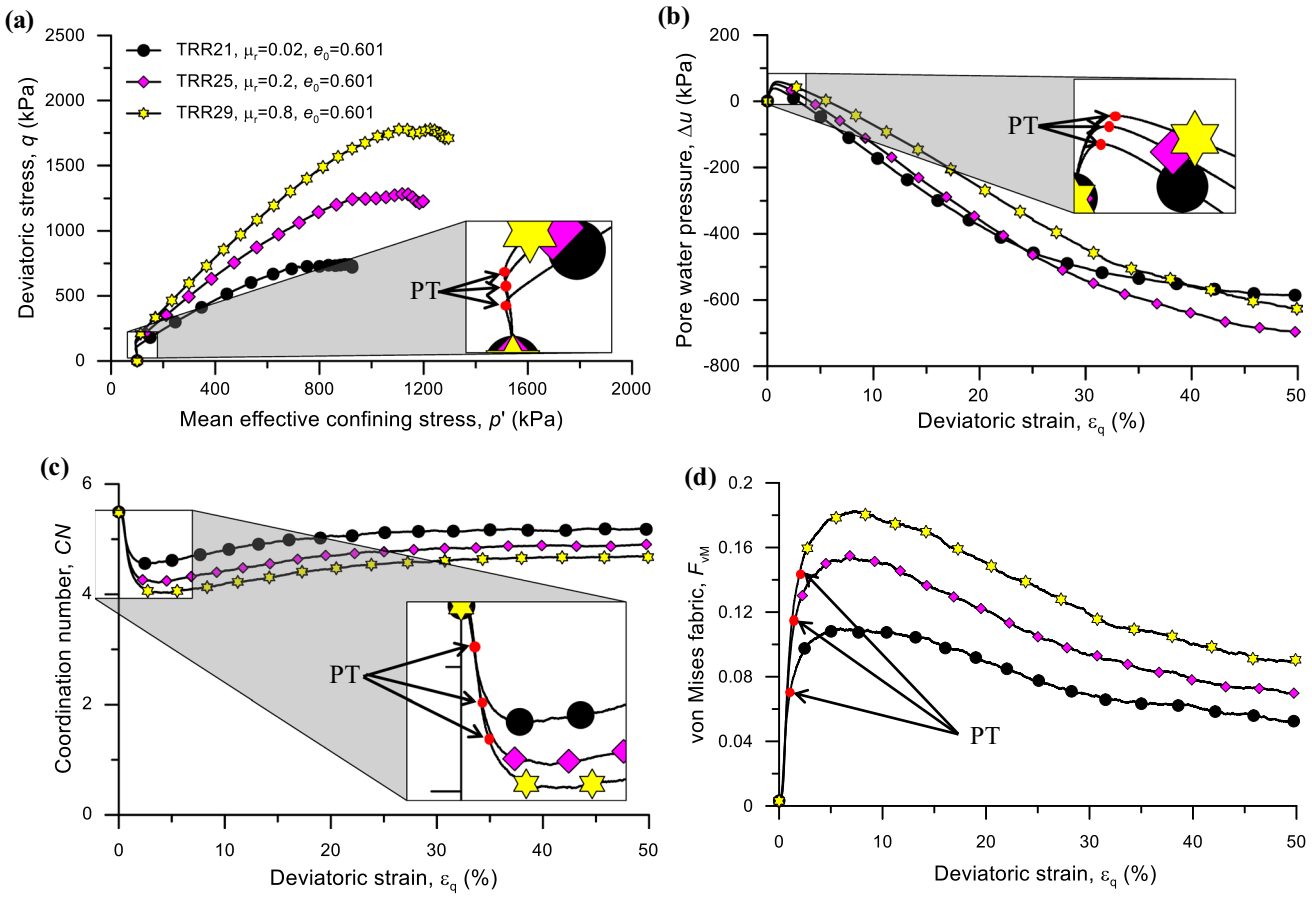

Fig. 9 Influence of μ_r on PT state: **a** at $dp' = 0$, and **b** $d\Delta u = 0$, **c** PT projected on *CN* evolution path, **d**PT projected on F_{vM} evolution path

[68] observed peak dilatancy to be independent of rolling resistance. In Fig. 10d, e the evolution of CN and F_{vM} during drained shearing is presented. The behaviour is identical to what is observed throughout CV simulations.

Similar to the PT state in undrained shearing, a characteristic state (ChS) exists in drained shearing which signifies the transition between contractive and dilative behaviour [38]. The ChS in $\varepsilon_v - \varepsilon_q$ space is presented in Fig. 11a. The ChS can be pinpointed as the state of $d\varepsilon_v = 0$, i.e. dilatancy, $d = d\varepsilon_v/|d\varepsilon_q| = 0$. Similar to the PT, the ChS is influenced by μ_r. The ChS occurred at larger ε_v and ε_q for specimens mobilised with large μ_r for specimens sheared with similar initial states. Thus, in both CV and drained shearing of medium dense/dense specimens, initial contractive tendencies were prolonged for assemblies mobilised with larger rolling resistance. It is likely, this is due to the unease of displacing strong interlocking contacts, and thus dense assemblies stay in a contractive state for longer, until contacts may be displaced at larger shear stresses.

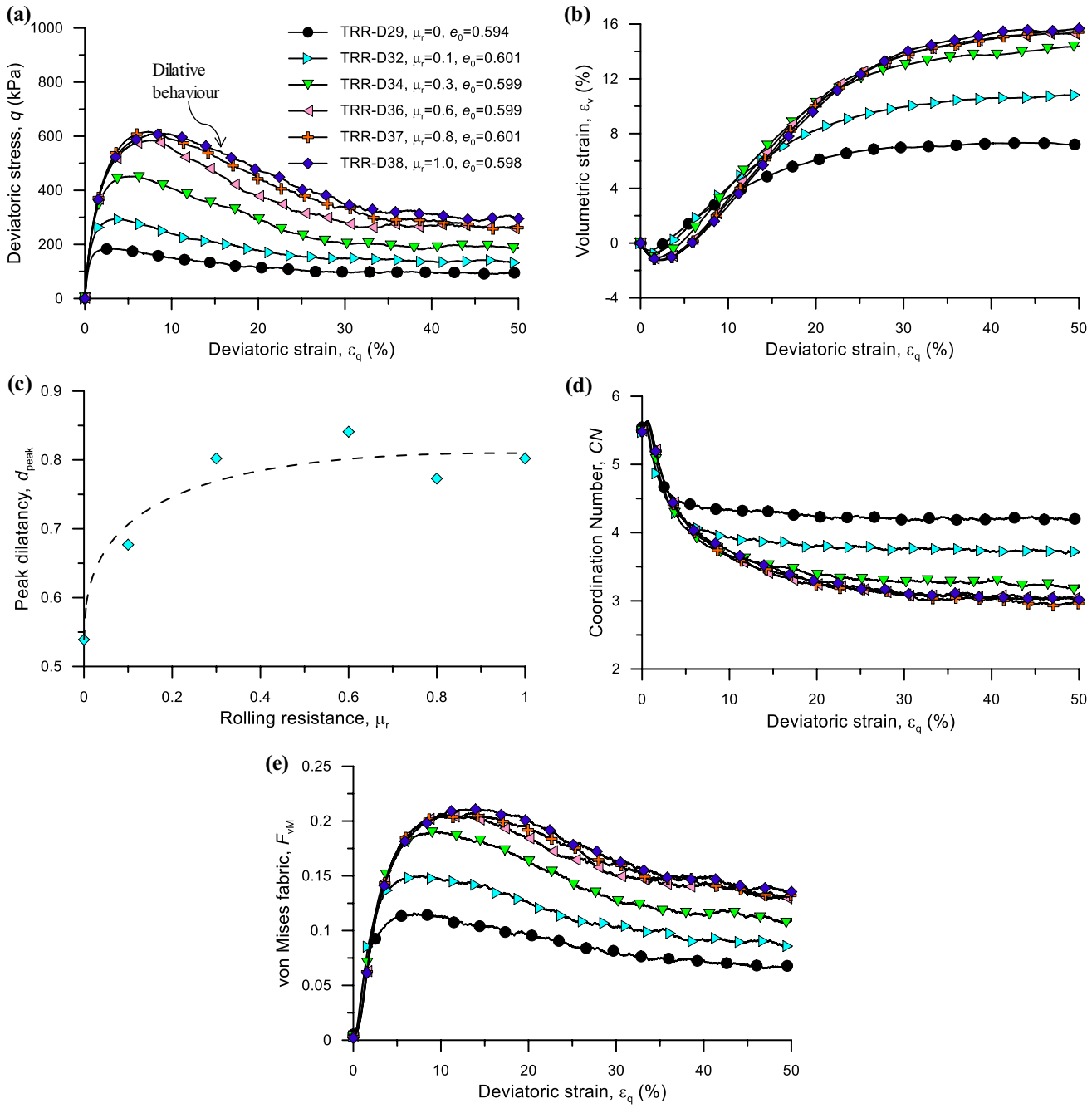

Fig. 10 Influence of μ_r on drained response of clean sand in **a** $q - \varepsilon_q$, **b** $\varepsilon_v - \varepsilon_q$, **c** $d_{peak} - \mu_r$, **d** $CN - \varepsilon_q$ and **e** $F_{vM} - \varepsilon_q$ spaces

The ChS point was projected on the *CN* and F_{vM} evolution paths (Fig. 11b, c). Similar to observations in CV shearing (Fig. 9), no change in soil micromechanics was observed at the ChS states in drained shearing. This supports the notion of continuum mechanics that the happening of PT and ChS states are related to the responses of dilative tendencies, not due to a change of particle contact density or particle spatial arrangement.

6 Critical state behaviour

6.1 Influence of rolling resistance on CSL

The CS data points from both CV and drained simulations with five different μ_r of 0, 0.1, 0.3, 0.5 and 0.7 are plotted in the e-log p' space as shown in Fig. 12a. The CSLs can be represented by the following power function as proposed by Li et al. [45]:

$$e_{cs} = e_{\lim} - \lambda\left(\frac{p'}{p_a}\right)^{\xi} \tag{8}$$

where p_a is the atmospheric reference stress i.e. $p_a = 100$ kPa and $e_{\lim}$, λ and ξ are dimensionless curve fitting parameters. The CSLs were independent of drainage condition aligning with early experimental studies [5, 9, 82, 90, 6, 71] and DEM studies [60]. These CSLs are curved and shifted upwards with increasing μ_r. Previous literature had suggested the curvature of the CSL to only be attributed to particle breakage (Konrad 1998). However, the DEM particles were unbreakable and therefore suggest otherwise—which is consistent with other DEM studies inheriting different contact models and particle shapes [59, 61, 62]. The pronunciation of the CSL curvature became more prominent at large μ_r values which led to merging CSLs at higher p' (> 1000 kPa) irrespective of μ_r. A conversing trend for CS data points at higher p' was also found with particle angularity in DEM [61]. However, Huang et al. [26, 28] using a simplified Hertz–Mindlin contact model where particle rotations were allowed (following Calvetti and Emeriault [7]) in DEM software LAMMPS found almost parallel CSLs with very mild curvature up to p' of 10,000 kPa for two frictional constraints. They also observed an unusual increase of critical state void ratio with increasing p' for $\mu \geq 0.5$. $\mu = 0.5$

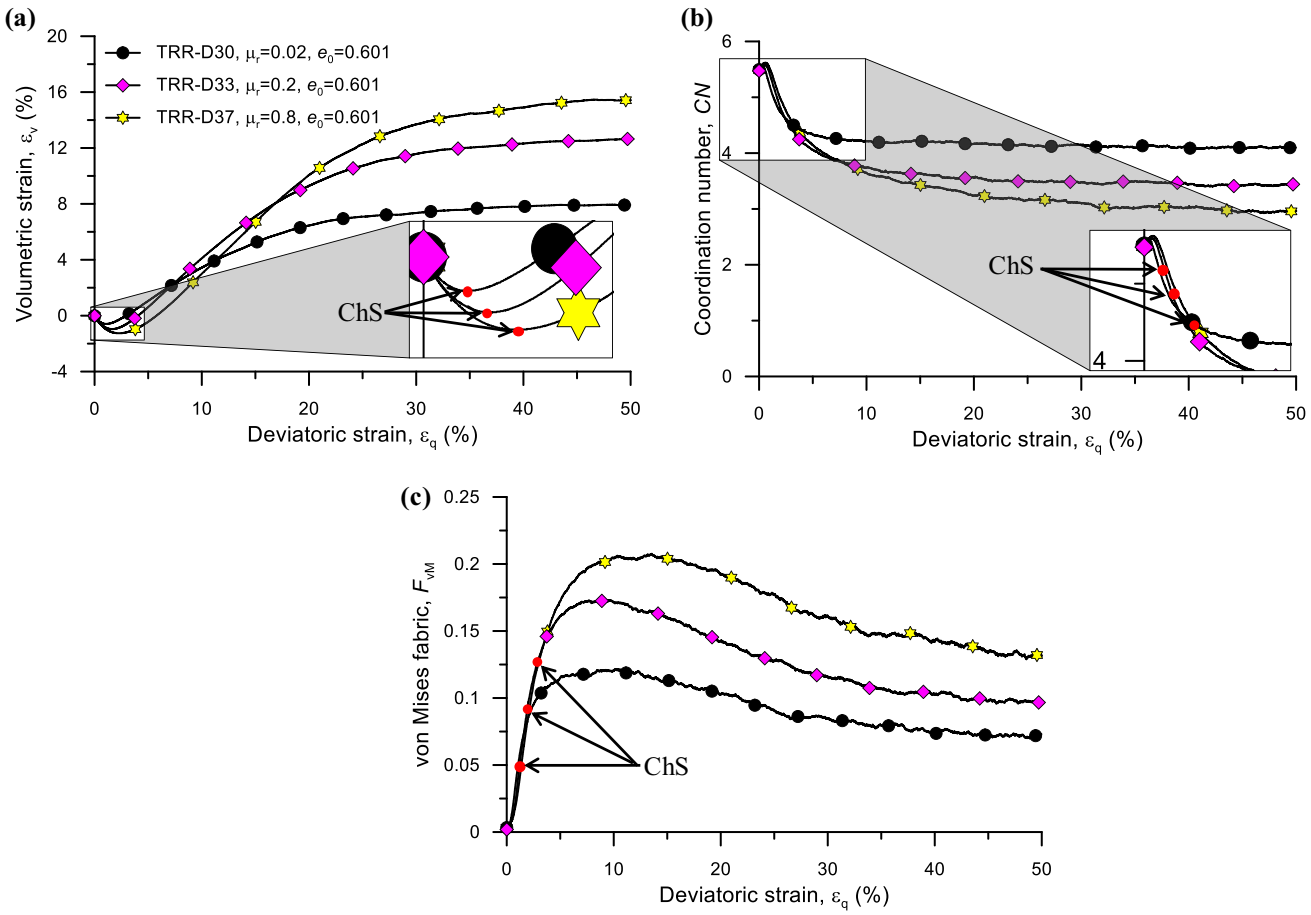

Fig. 11 Influence of rolling resistance on ChS

was used in this study and the unusual behaviour was not observed. Such difference with this study may be attributed to the difference in contact models, implementation platform i.e. PFC & LAMMPS and limited CS data in Huang et al. [26, 28]. The CS data points for other μ_r values are also projected with these CSLs in Fig. 12b. The data suggests there is negligible influence of μ_r on CSL in the e-log p' space when $\mu_r \geq 0.4$ and one CSL may be assumed in this range of μ_r.

The CSLs in the $q-p'$ space were also μ_r-dependant (Fig. 12c). Within the range of $0 \leq \mu_r \leq 1$, M increased from 0.73 to 1.38 with a noticeable change from 0.73 to 1.15 for μ_r only increased from 0.0 to 0.3. The increasing trend of M with μ_r is very similar to increasing M with increasing particle angularity in DEM [61]. Therefore, rolling resistance between particles contribute to the CSLs and its curvature in the e-log p' space in a similar manner to particle shape and thus, μ_r may be inferred as contributor to frictional properties of particle shape.

6.2 Change in CS behaviour with μ_r

A series of CV and drained simulations, where shearing commenced from similar initial states ($p'_0 = 100$ kPa, $e_0 = 0.5975 \pm 0.0035$) for both drained and CV simulations were performed and the influence of rolling resistance on q, CN and F_{vM} at CS was captured (Fig. 13). The change in μ_r with the three quantities are similar between drainage conditions. In Fig. 13a, q at CS (q_{cs}) increases gradually with μ_r before plateauing at approximately $\mu_r = 0.4$. Thus, at larger μ_r ranges the influence of particle rolling resistance on q_{cs} is negligible. Similar tendencies were also observed for CN and F_{vM} in Fig. 13b, c respectively. Although strictly not a threshold μ_r value, the change in CS behaviour becomes relatively unnoticeable as $\mu_r \rightarrow 1$. Liu et al. [46] reported a threshold μ_r value of 0.3 where at $\mu_r \geq 0.3$ the strength of granular material shows negligible change. Similar is observed here, although micromechanical entities CN and F_{vM} are observed to change differently at $\mu_r \geq 0.3$. Therefore, a threshold rolling value may only be applicable for selected entities/performance parameters rather than applying for the entire material response. Further, it should be acknowledged that the change in contact

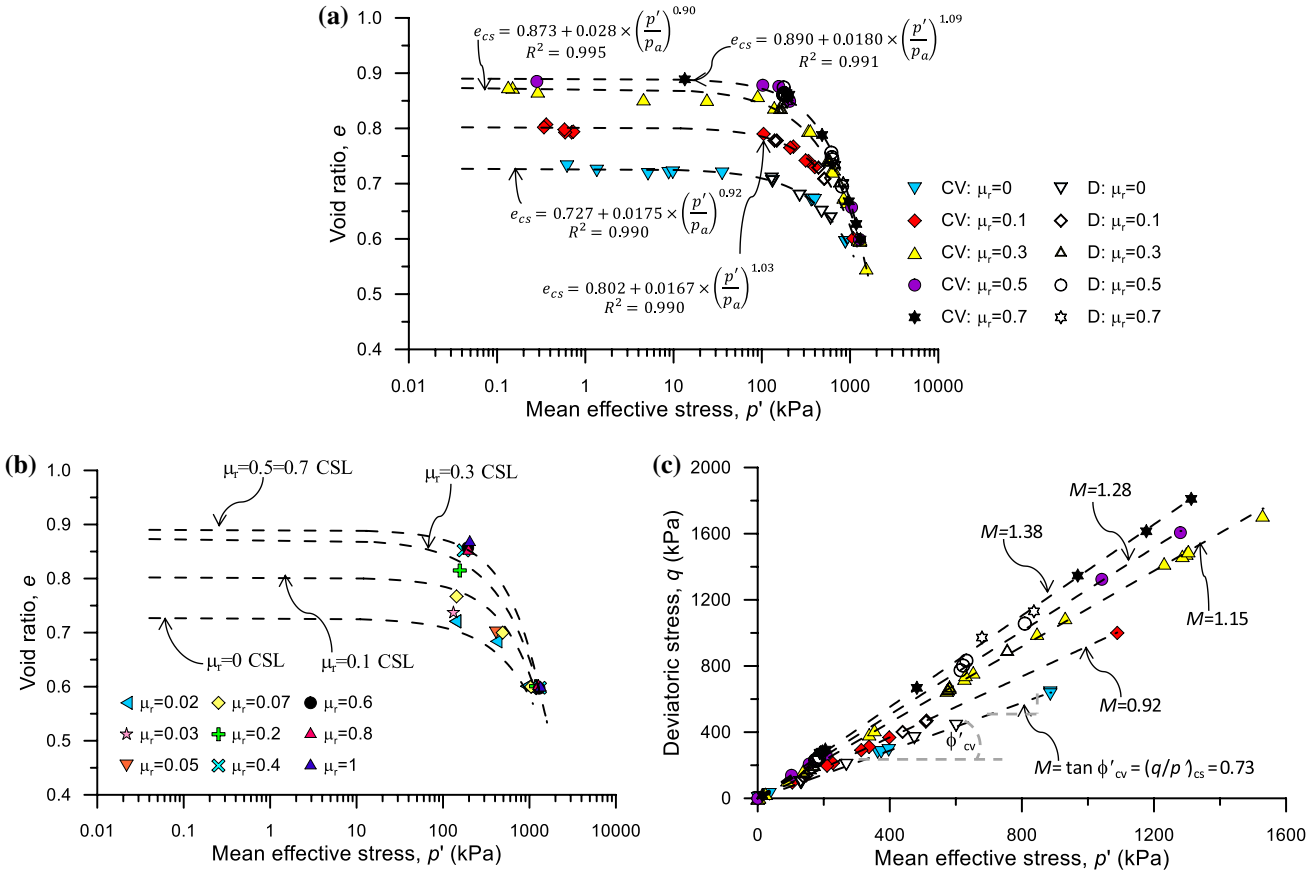

Fig. 12 Influence of μ_r on CS response of clean sand **a** influence on q_{cs}, **b** influence on CN_{cs}, **c** influence on $F_{vM(cs)}$

model (e.g. contact stiffness algorithms) and model parameters (e.g. μ) which may influence particle rolling behaviour may lead to different observations relating to a threshold μ_r value.

6.3 Rolling resistance and associated micro-mechanics for CSL

Both linear [22] and power [58] functions have been used to express the relationship between CN and p' at CS. Providing a better fit for the data in this study, a power function was used:

$$CN_{cs} = A + B \times \left(\frac{p'}{p_a}\right)^C \tag{9}$$

where CN_{cs} is the CN at CS and A, B and C are fitting constants. A strong relation between p' and CN_{cs} for each μ_r value, irrespective of drainage condition was observed (see Fig. 14a). For any given p'_{cs} value the CN_{cs} decreased with increasing μ_r. In Fig. 14b, the contact networks of two assemblies, TRR10 and T14, which possess μ_r values of 0 and 0.3, but similar p'_{cs} values reflect this change in contact density. The contact network for TRR10 relies on a larger number of weak contacts to achieve a similar CS strength when compared to T14. For specimen TRR10, $p'_{cs} = 363$ kPa is achieved via widespread weak contact forces which may be easily displaced or rearranged, whilst T14 achieves $p'_{cs} = 354$ kPa through the efficient formation of strong contact forces which possess larger shear resistance. Ultimately, a change in rolling tendencies substantially impacts fabric related entities such as contact orientation and contact intensity at CS.

For all CV and drained simulations, the $F_{vM(cs)}$ behaviour was captured by CSLs in $F_{vM} - \log p'$ space (Fig. 15). No influence of drainage condition on observed CS fabric behaviour. Firstly, it is encouraging that CS fabric behaviour is analogous with overall observed CS behaviour, e.g. CSL in $e - \log p'$ space—further showing fabric is highly influential on soil behaviour and advancing the theory that fabric should be encapsulated under CSSM framework [41]. The CSL in $F_{vM} - \log p'$ space shifted upwards with μ_r. Huang et al. [26, 28] observed identical behaviour, with the case of μ. The increasing anisotropy with μ_r may be explained by

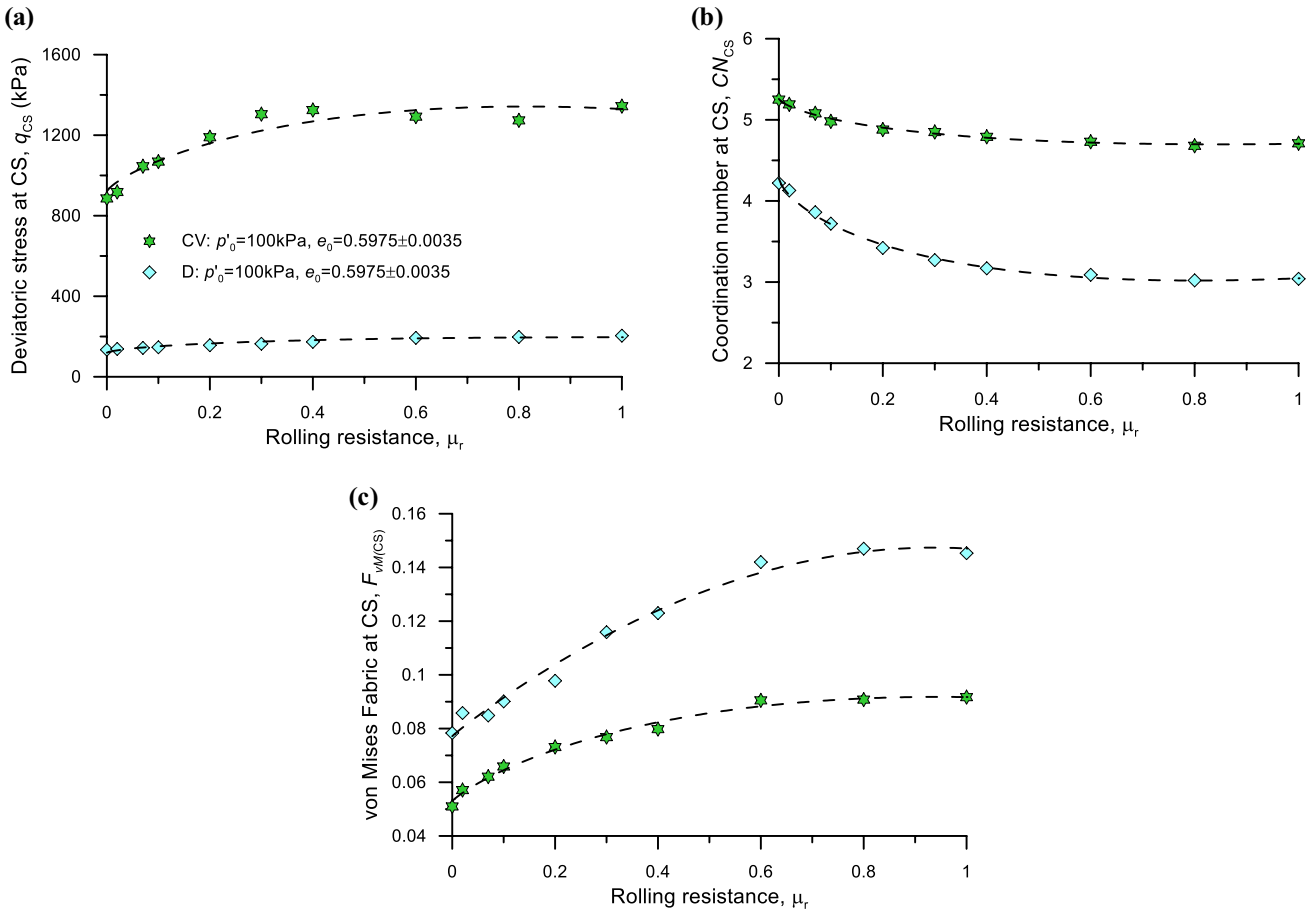

Fig. 13 Effect of μ_r on CSL in **a** e-log(p') space, **b** projected data in e-log(p') space and **c** $q - p'$ space

the intensification of strong contact formation (observed in Fig. 7), which primarily contributes to the deviatoric stress (and therefore likely deviatoric fabric) component of the assembly [52, 72].

7 Particle rotation and angular velocity

In PFC^{3D}, the angular velocity, which represents rotational tendency of individual particles, can be captured throughout shearing. At prescribed ε_q values, the angular velocity for each particle was recorded and the average angular velocity, ω_{avg} of the entire assembly was calculated. In Fig. 16, the variation of ω_{avg} and average angular velocity at critical state, ω_{cs} for a series of drained shearing tests (with similar initial states, i.e. $p'_0 = 100$ kPa and $e_0 = 0.5975 \pm 0.0035$) are plotted against rolling resistance. A very strong relationship between μ_r and ω_{avg} was observed. Low rolling resistance corresponded to high particle rotations and vice versa. The observations indicate ω_{avg} can be used within DEM to quantify rolling behaviour. From herein, ω_{avg} is used as an indirect measure to capture particle rolling tendencies.

In Fig. 17a, the influence of e_0 and p'_0 on the rotational tendencies of granular material is assessed. All specimens had $\mu_r = 0.1$ and exhibited NF behaviour (Fig. 17b). Although unpronounced, a trend in Fig. 17 is that during strain hardening, ω_{avg} increases. Further, particle rolling was observed to increase with e_0 (on comparison between TRR34 and TRR35), i.e. rolling is more prone to occur in loose specimens. The influence of p'_0 on rolling tendencies (on comparison of TRR35 and TRR38) is negligible.

In Fig. 18, the variation of ω_{avg} is plotted against the post-compression state parameter, ψ_0 for $\mu_r = 0.1$ and $\mu_r = 0.3$. Notably, contractive specimens with higher ψ_0 corresponded to large rotational/rolling behaviour. In dilative specimens rolling/rotational behaviour still existed although tendencies were minimised. The trend line shifts downwards in the $\omega_{avg} - \psi_0$ space as μ_r increased. Thus, depending on μ_r, each $\omega_{avg} - \psi_0$ possesses its own characteristic rolling tendency.

8 Influence of rolling resistance on instability state

Instability triggering is a state which corresponds to the peak q in undrained shearing before strain softening occurs and is also known to be the onset of static liquefaction. The instability state is a characteristic feature of undrained behaviour of loose sand. It has been characterised using approaches, such as the collapse line (CL) [82] or the instability line (IL) [13, 37]. Perhaps the instability stress ratio, $\eta_{IS} = (q/p')_{peak}$ is better suited to quantify instability behaviour as it can be linked with mechanical performance parameters such as ψ_0 [53, 87, 39]. Yang [87] developed an exponential relationship and Rahman and Lo [53] modified the relationship between η_{IS} and ψ in the form of:

$$\eta_{IS} = A + \exp(-B\psi) \tag{10}$$

where A and B are curve fitting parameters. Equation (10) captures the instability behaviour as a function of soil state. In Fig. 19a the relationship between η_{IS} and ψ_0 for varying μ_r values is captured. The instability data points in the $\eta_{IS} - \psi_0$

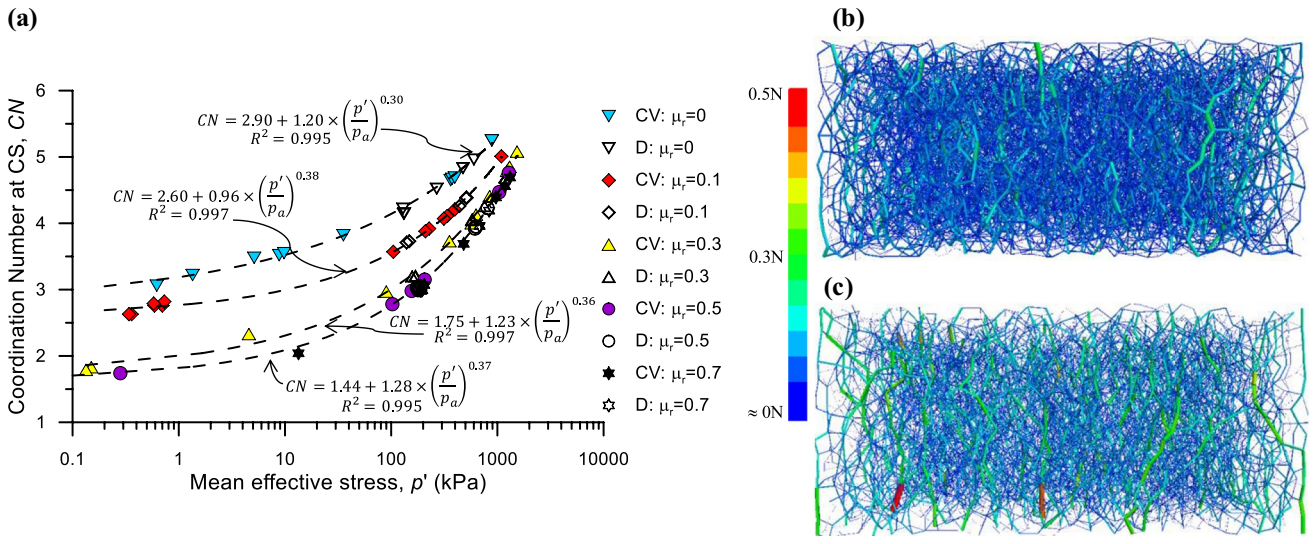

Fig. 14 **a** Influence of μ_r on CN_{CS} in CN-log (p') space, **b** Specimen TRR10 ($\mu_r = 0$) contact force network, **c** Specimen T14 ($\mu_r = 0.3$) contact force network

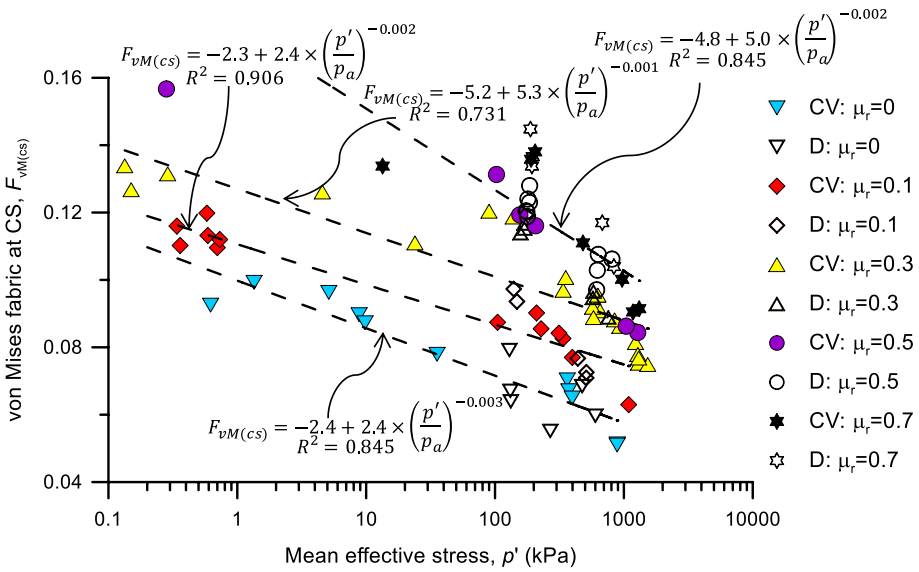

Fig. 15 Influence of μ_r on CS behaviour in $F_{vM} - \log(p')$ space

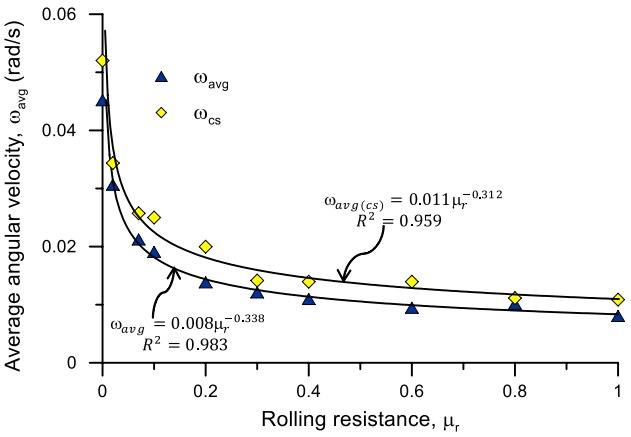

Fig. 16 Particle angular velocity as a function of μ_r

space showed a clear upward shift with increasing μ_r. However. in the free-rolling case, a steeper reduction in η_{IS} occurs than those assemblies mobilised with a finite μ_r. Through a reanalysis of DEM data, Nguyen et al. [59] asserted a steep slope in $\eta_{IS} - \psi_0$ space to be attributed to low particle angularity and interlocking capabilities. Aligning with the force chain networks in Fig. 7 it can be suspected that the steep behaviour shown for $\mu_r = 0$ is also due to poor interlocking and highly lubricative behaviour. Therefore, a link between particle angularity and rolling resistance share a relation may be made between the two studies. That is, it is possible that μ_r can be used as a tuneable parameter in DEM to indirectly control particle angularity.

When the F_{vM} at η_{IS}, $F_{vM(IS)}$ is plotted against ψ_0 (Fig. 19b), two separate relationships are yielded. Following

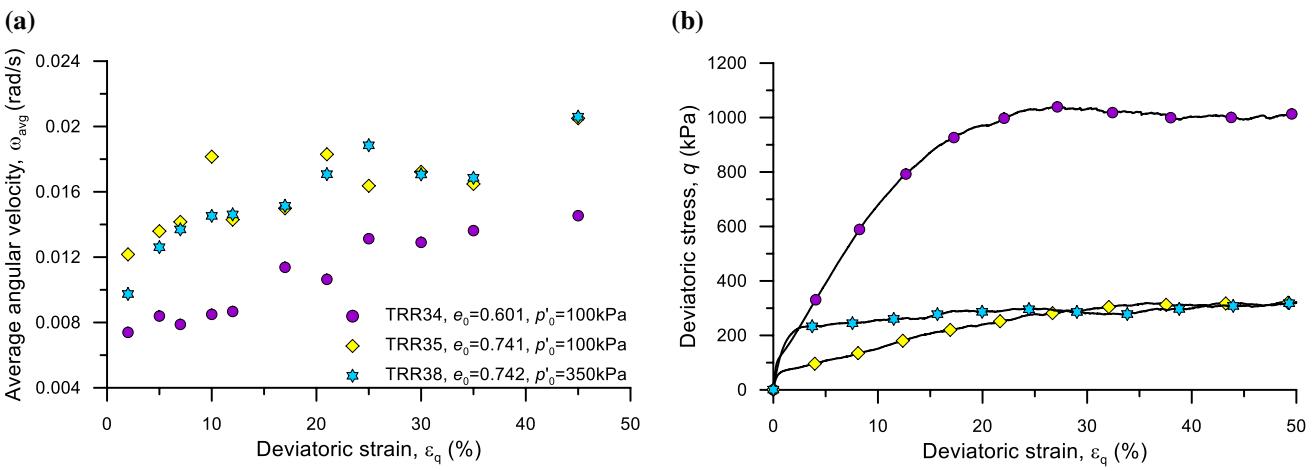

Fig. 17 **a** Influence of ω_{avg} on e_0 and p'_0 **b** strain hardening behaviour of TRR34, TRR35 & TRR38

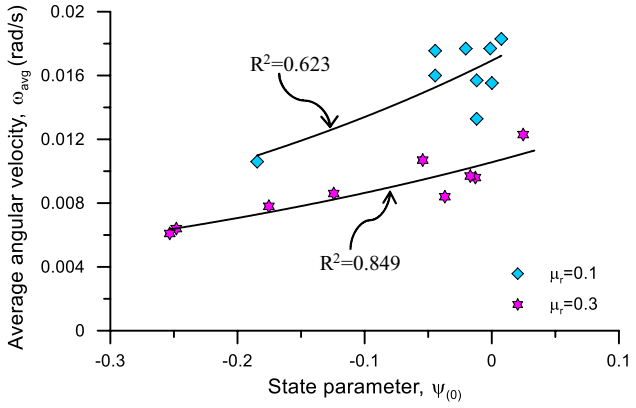

Fig. 18 Influence of rotational tendencies on material state

on from Fig. 19a, when $\mu_r = 0$, a steeper decrease of $F_{vM(IS)}$ occurs with increasing ψ_0, in comparison to those assemblies mobilised with a finite μ_r value. Thus, for $\mu_r = 0$ the behaviour observed in $\eta_{IS} - \psi_0$ is reflected in $F_{vM(IS)} - \psi_0$ space. Again, this behaviour could be attributed to the associated low interlocking capabilities. Secondly, when $\mu_r > 0$ the influence of μ_r on $F_{vM(IS)}$ appears to be nullified. In fact, a single trend line can be approximated to represent the trend in $F_{vM(IS)} - \psi_0$.

9 Influence of rolling resistance on PT and ChS

Both PT and ChS states correspond to the change over from contractive to dilative tendency and, therefore, they can be assumed as a state of zero dilatancy and equivalent. Thus, the dilatancy equation of SANISAND model [43] can be manipulated to derive the following relation between stress ratio at PT (η_{PT}) and ChS (η_{ChS}) with ψ –

$$\eta_{PT/ChS}/M = \exp(-B\psi) \tag{11a}$$

However, some experimental studies suggested the equivalence between η_{PT} and η_{ChS} [12, 40], whilst others observed different behaviour [92]. Therefore, the equivalence of these states and the functional relation has significant importance in granular material modelling.

It is found in Fig. 20a that assemblies with large rolling resistance possesses larger η_{PT} or η_{ChS} at the same ψ_0, however both η_{PT} and η_{ChS} possess single relation with ψ_0 for each μ_r i.e. η_{PT} and η_{ChS} are equivalent. When η_{PT} and η_{ChS} were normalised by M (Fig. 20b), a single trend line is developed, further indicating the equivalence of η_{PT} and η_{ChS}, and support normalisation in constitutive relation. However, the best fit function is slightly different than Eq. (11) and presented as below:

$$\eta_{PT/ChS}/M = A\exp(-B\psi) \tag{11b}$$

While this observation confirms the relationship between characteristic features with ψ_0 in the state-dependent constitutive modelling [43], it also indicates possible adjustment. The deviatoric fabric at PT and ChS states, $F_{vM(PT/ChS)}$ (normalised with M) also shared a unique relation with ψ_0, irrespective of μ_r (Fig. 20c).

10 Conclusions

A series of CV and drained triaxial simulations were undertaken using the RRLCM within PFC^{3D}. The influence of particle rolling on clean sand behaviour was captured through the CSSM framework. The key conclusions drawn from the study are summarised below:

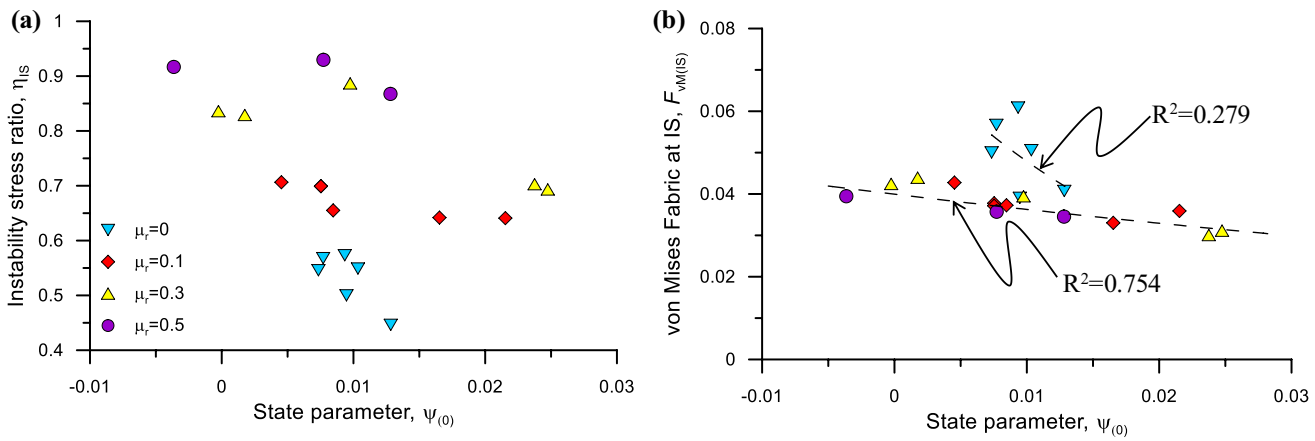

Fig. 19 Influence of particle rolling on instability behaviour **a** $\eta_{IS} - \psi_0$, **b** $F_{vM(IS)} - \psi_0$ spaces

i. Rolling resistance has significant influence on the observed behaviour of granular material. Assemblies mobilised with high rolling resistance possessed highly frictional behaviour with dilative tendencies. Assemblies with low rolling resistance manifested less dilative tendencies. Thus, the dilative tendency shared a dependency with μ_r. Although, at approximately $\mu_r > 0.3$, the influence of μ_r on volume dilation and peak dilatancy was almost unnoticeable.

ii. Strong contact formation thrived for assemblies mobilised with large rolling resistance inferring that interlocking behaviour is influenced by rolling tendencies/resistance. A potential by-product of the strong contact formation is strain softening or brittle failure after peak deviatoric stress, q. Assemblies mobilised with low rolling resistance were incapable of forming strong interlocking contacts and instead yielded contact networks that were rife with weak contact forces. μ_r could therefore be used as a parameter to indirectly control the interlocking capabilities of a granular assembly.

iii. The influence of μ_r on characteristic features of undrained shearing (i.e. PT and η_{IS}) and drained shearing (i.e. ChS) were captured. For dense/medium-dense specimens, initial contractive tendencies were prolonged in terms of deviatoric strain (ε_q) for assemblies mobilised with large rolling resistance. The stress ratio (q/p') at PT, ChS and instability states, i.e. η_{PT}, η_{Ch} and η_{IS} respectively, were all shown to increase with μ_r. η_{PT}, η_{ChS} and η_{IS} also showed correlations with ψ_0 for different values of μ_r. The study observed an equivalence between η_{PT} and η_{ChS}.

iv. CS parameters were significantly influenced by particle rolling. The CSL in e-log p' space shifted upwards when rolling resistance increased. When μ_r was large, the curvature of the CSL became increasingly pronounced. Thus, the geometry of the CSL was influenced by rolling behaviour rather than particle breakage, which was suggested in the literature. An increase of M was observed with μ_r. Although at large ranges of μ_r, even though M continued to increase, changes in

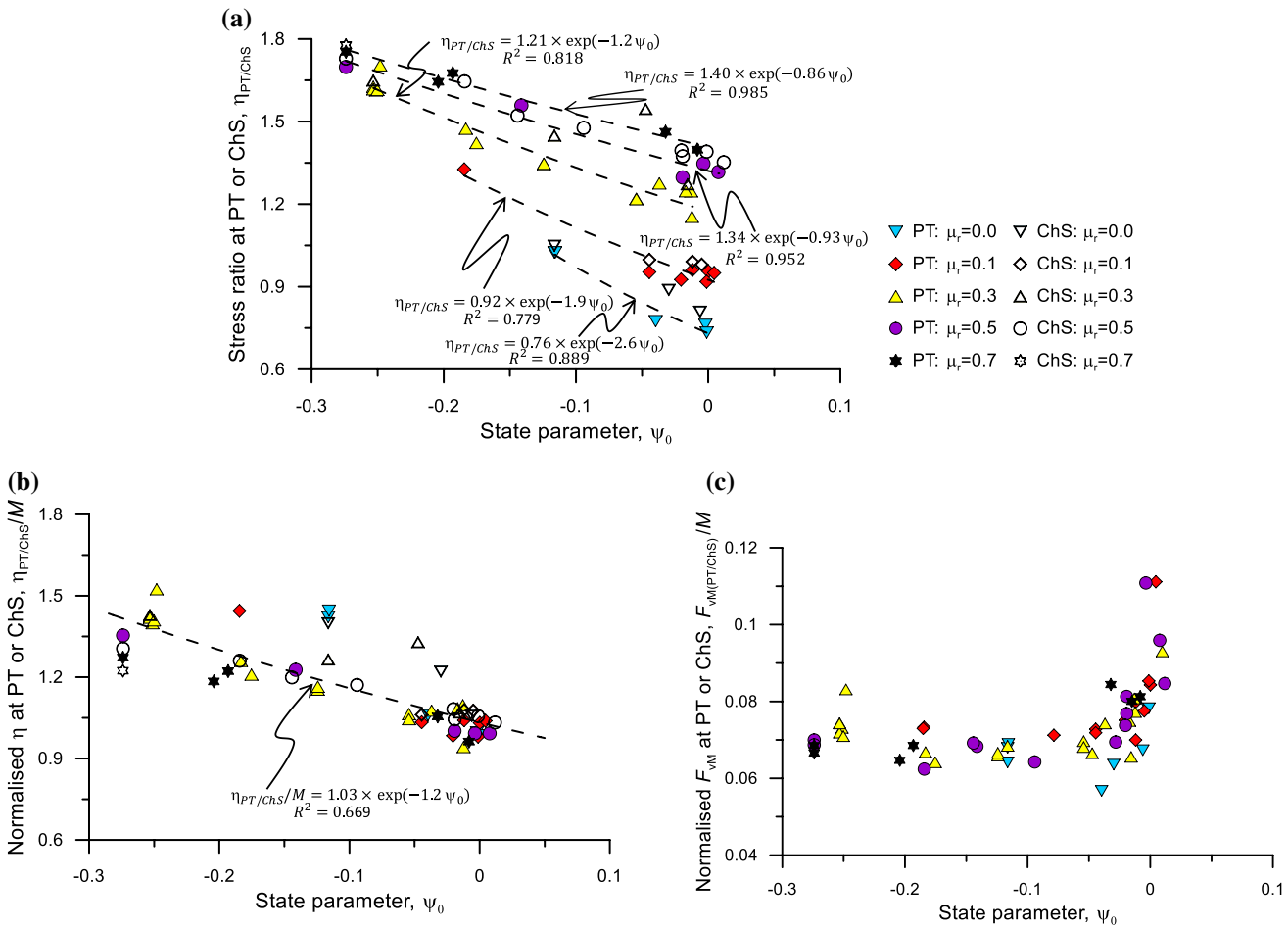

Fig. 20 Influence of particle rolling in **a** $\eta_{PT/ChS} - \psi_0$, **b** $\eta_{PT/ChS}/M - \psi_0$ and **c** $F_{vM(PT/ChS)}/M - \psi_0$ spaces

other mechanical entities such as F_{vM}, CN, q and the CSL in e-log p' space were mostly unnoticeable.

v. A larger deviatoric fabric was observed with increasing μ_r. $F_{vM(IS)}$ and $F_{vM(PT)}$ showed relationships with initial state parameter (ψ_0) with respect to μ_r.

Although the study presents valuable DEM findings relating to the influence of particle rolling on the characteristic (undrained and drained) behaviour of granular material, it should be noted that several rolling resistance models/frameworks exist, as noted in Ai et al. [2]. Utilising a rolling resistance model/algorithm which differs from that used in this study may lead to observed behaviour which diverges from the observations in this study. The influence of particle rolling on soil behaviour has been isolated in the manuscript, although sliding and twisting behaviour which occurs at the contact may also influence granular material behaviour.

Acknowledgements The first author acknowledges the support provided by the Research Training Program domestic (RTPd) scholarship, awarded by The School of Natural and Built Environments, University of South Australia.

Compliance with ethical standards

Conflict of interest The authors declare that they have no conflict of interest.

Appendix A: Method of deformability

Computation of stiffness parameters

Through the method of deformability:

$$k_n = \frac{AE^*}{L} \tag{12}$$

$$k_s = \frac{k_n}{k^*} \tag{13}$$

$$k_r = k_s R_r \tag{14}$$

here $A = \pi r^2$ represents the contact area. Depending on the type of entities in contact r is computed:

$$r = \begin{cases} \min\left(R^{(1)}, R^{(2)}\right), \textit{for particle} - \textit{particle contacts} \\ R^{(1)}, \textit{for particle} - \textit{wall contacts} \end{cases} \tag{15}$$

where $R^{(1)}$ denotes the radius of contact entity 1. In similar nature the contact length (L) is computed based on contact type:

$$L = \begin{cases} R^{(1)} + R^{(2)}, \textit{for particle} - \textit{particle contacts} \\ R^{(1)}, \textit{for particle} - \textit{wall contacts} \end{cases} \tag{16}$$

E^* and $k^* = k_n/k_s$ are input parameters in the study and are discussed and presented in Table 1 in the manuscript. The rolling radius, R_r and its formulation is also presented in the manuscript.

Appendix B: Rolling resistance linear contact model

The rolling resistance linear contact model (RRLCM) utilised in this study adds to the conventional linear contact model commonly used in DEM through the installation of a rolling spring and dashpot at the contact (Fig. 21).

In a rheological sense, the rolling spring signifies the presence of an elastic resisting moment between contacting pieces (M_r^k), whilst the dashpot signifies the presence of a viscous moment at the contact (M_r^d). The overall rolling resistance moment (M_r) may be mathematically defined as:

$$M_r = M_r^k + M_r^d \tag{17}$$

to effectively utilize the RRLCM in a numerical modelling environment, M_r must be updated incrementally with respect to the time step. At time $t + \Delta t$, M_r^k may be computed via:

$$M_{r,\Delta t+t}^k = \begin{cases} M_{r,t}^k + \Delta M_r^k \\ \left|M_{r,t+\Delta t}^k\right| \le M^* \end{cases} \tag{18}$$

here M^* represents the maximum (limiting) resisting torque ($M^* = \mu_r \bar{R} F_n$) and $\bar{R} = \left(r_i r_j\right)/\left(r_i + r_j\right)$; where F_n is the normal contact force, $\bar{R}$ represents the effective radius of the contact, r_i and r_j are the radii of contacting entities. When a boundary or wall element is the contacting entity, $r \to \infty$. Notice, when $\mu_r = 0$, $M^* = 0$ and therefore a free-rolling environment is created. M_r^k is the incremental rolling resistance torque observed at time, $t + \Delta t$ and is computed through consideration of the rolling stiffness, k_r and the relative rotation between two contacting particles, θ_r,

$$\Delta M_r^k = -k_r \Delta \theta_r \tag{19}$$

where $k_r = k_s R_r$. A limitation of the model is defining a k_r which has strong physical basis. k_r is related to k_s based on an idealized consideration that the moment generated at a contact due to shear displacement is equivalent to the moment generated due to rolling displacement. M_r^d in Equation 17 is also updated with respect to the time step, $t + \Delta t$:

$$M_{r,t+\Delta t}^d = \begin{cases} -C_{rr} \; if \left|M_{r,t+\Delta t}^k\right| < M^* \\ 0 \; if \left|M_{r,t+\Delta t}^k\right| = M^* \end{cases} \tag{20}$$

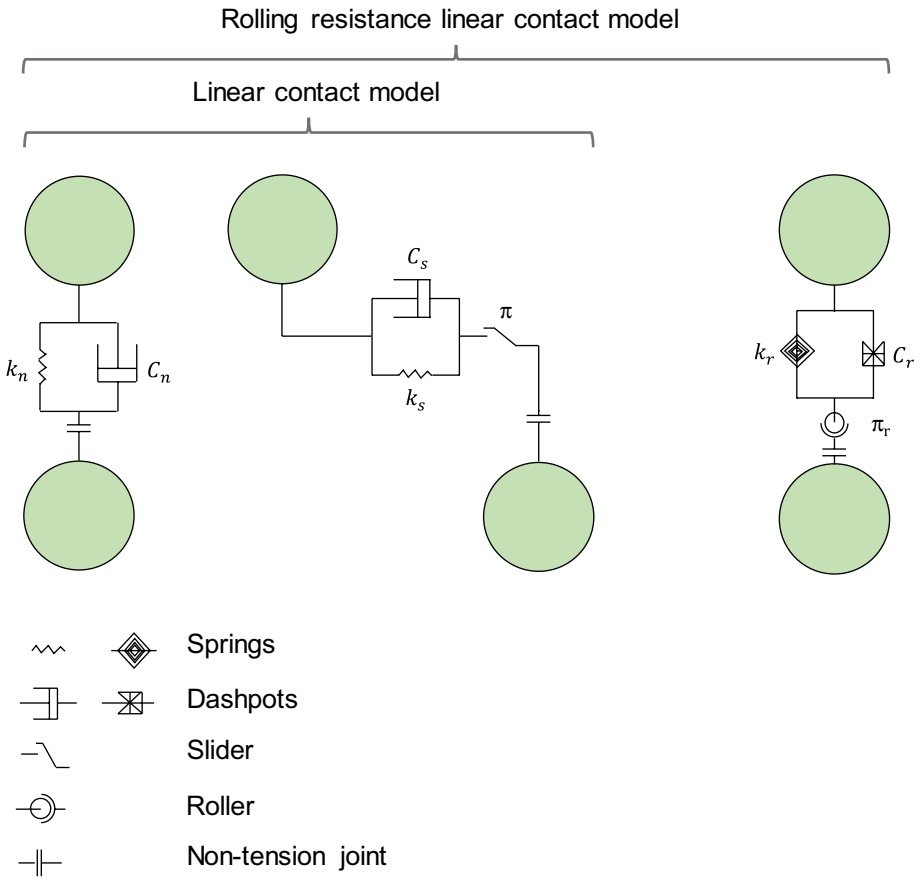

Fig. 21 Rolling resistance linear contact model. After Iwashita and Oda [32]

where $C_r = 2_r\sqrt{I_r k_r}$ is the viscous damping rolling coefficient, η_r is the critical viscous damping ratio and I_r is the equivalent moment of inertia about the contact point between two contacting entities. Instead of an oscillating resisting moment applied at the contact, as applied in some rolling resistance contact models [2], the applied resisting moment at the contact within a quasi-static system is stable and therefore the packing behaviour of the assembly is stabilized. For such reasons, this model is often used in DEM simulation of quasi-static systems. Using various modified versions of this model in DEM along with the tuning of μ_r, some have captured the influence of particle rolling on the behaviour of granular material in triaxial compression. In particular some observed that with the addition of rolling resistance, shear strength and dilatancy increases [32, 46, 54, 94], shear banding and strain localization intensifies [32, 33, 54, 84] and fabric anisotropy intensifies [46].

References

1. Aboul Hosn, R., Sibille, L., Benahmed, N., Chareyre, B.: Discrete numerical modeling of loose soil with spherical particles and interparticle rolling friction. Granular Matter **19**(1), 1–12 (2017)
2. Ai, J., Chen, J., Rotter, M., Ooi, J.Y.: Assessment of rolling resistance models in discrete element simulations. Powder Technol. **206**, 269–282 (2011)
3. Barnett, N., Rahman, M.M., Karim, M.R., Nguyen, H.B.K., Carraro, J.A.H.: Equivalent state theory for sand with non-plastic fine mixtures: a DEM investigation. In press, Geotechnique (2020)
4. Been, K., Jefferies, M.G.: A state parameter for sands. Geotechnique **35**(2), 99–112 (1985)
5. Been, K., Jefferies, M.G., Hachey, J.: The critical state of sands. Geotechnique **41**(3), 365–381 (1991)
6. Bobei, D.C., Wanatowski, D., Rahman, M.M., Lo, S.R., Gnanendran, C.T.: The effect of drained pre-shearing on the undrained behaviour of loose sand with a small amount of fines. Acta Geotech. **8**(3), 311–322 (2013)
7. Calvetti, F., Emeriault, F.: Interparticle forces distribution in granular materials: link with the macroscopic behaviour. Mech. Cohes-Frict. Mat. **4**(3), 247–279 (1999)
8. Carrera, A., Coop, M., Lancellotta, R.: Influence of grading on the mechanical behaviour of stava tailings. Geotechnique **61**(11), 935–946 (2011)
9. Casagrande, A.: Liquefaction and cyclic deformation of sands. In: 5th Pan American conference on soil mechanics Buenos Aires, pp. 80–133 (1975)
10. Chang, X., Wang, Y., Zhou, W., Ma, G., Liu, J.: The influence of rotational resistance on critical state of granular materials.

In: Proceedings of the 7th International Conference on Discrete Element Methods (2016)
11. Christoffersen, J., Mehrabadi, M.M., Nemat-Nasser, S.: A micromechanical description of granular material behavior. J. Appl. Mech. **48**(2), 339–344 (1981)
12. Chu, J.: An experimental examination of the critical state and other similar concepts for granular soils. Can. Geotech. J. **32**(6), 1065–1075 (1995)
13. Chu, J., Leong, W.K.: Effect of fines on instability behaviour of loose sand. Geotechnique **52**(10), 751–755 (2002)
14. Cundall, P.A., Strack, O.D.L.: A discrete numerical model for granular assemblies. Geotechnique **29**(1), 47–65 (1979)
15. da Cruz, F., Emam, S., Prochnow, M., Roux, J.-N., Chevoir, F.: Rheophysics of dense granular materials: discrete simulation of plane shear flows. Phys. Rev. E **72**(2), 021309 (2005)
16. Dafalias, Y.F., Taiebat, M.: SANISAND-Z: zero elastic range sand plasticity model. Geotechnique, 1–15 (2016)
17. Estrada, N., Taboada, A., Radjaï, F.: Shear strength and force transmission in granular media with rolling resistance. Phys. Rev. E Stat. Nonlinear Soft Matter Phys. **78**(2), 021301–021301 (2008)
18. Fonseca, J., O'Sullivan, C., Coop, M., Lee, P.D.: Quantifying the evolution of soil fabric during shearing using directional parameters. Geotechnique **63**(6), 487–499 (2013)
19. Fonseca, J., O'sullivan, C., Coop, M.R., Lee, P.D.: Non-invasive characterization of particle morphology of natural sands. Soils Found. **52**(4), 712–722 (2012)
20. Frossard, E.: Effect of sand grain shape on interparticle friction; indirect measurements by Rowe's stress dilatancy theory. Geotechnique **29**(3), 341–350 (1979)
21. Fu, P., Dafalias, Y.F.: Fabric evolution within shear bands of granular materials and its relation to critical state theory. Int. J. Numer. Anal. Meth. Geomech. **35**(18), 1918–1948 (2011)
22. Gu, X., Huang, M., Qian, J.: DEM investigation on the evolution of microstructure in granular soils under shearing. Granular Matter **16**(1), 91–106 (2014)
23. Guo, N., Zhao, J.: The signature of shear-induced anisotropy in granular media. Comput. Geotech. **47**, 1–15 (2013)
24. Guo, P., Su, X.: Shear strength, interparticle locking, and dilatancy of granular materials. Can. Geotech. J. **44**(5), 579–591 (2007)
25. Hasan, A., Alshibli, K.A.: Experimental assessment of 3D particle-to-particle interaction within sheared sand using synchrotron microtomography. Geotechnique **60**(5), 369–379 (2012)
26. Huang, X., Hanley, K.J., O'Sullivan, C., Kwok, C.Y.: Exploring the influence of interparticle friction on critical state behaviour using DEM. Int. J. Numer. Anal. Meth. Geomech. **38**(12), 1276–1297 (2014)
27. Huang, X., Hanley, K.J., O'sullivan, C., Kwok, C.-Y.: Implementation of rotational resistance models: a critical appraisal. Particuology **34**, 14–23 (2017)
28. Huang, X., O'sullivan, C., Hanley, K.J., Kwok, C.Y.: Discrete-element method analysis of the state parameter. Geotechnique, 954–965 (2014)
29. Ishihara, K.: Liquefaction and flow failure during earthquakes. Geotechnique **43**(3), 351–415 (1993)
30. Isomokos, A., Georgiannou, V.: Effect of grain shape and angularity on the undrained response of fine sands. Can. Geotech. J. **47**(5), 539 (2010)
31. Itasca: Particle Flow Code in 3 Dimensions (PFC3D) Version 4. Minnesota, USA (2008)
32. Iwashita, K., Oda, M.: Rolling resistance at contacts in simulation of shear band development by DEM. J. Eng. Mech. **124**, 285–292 (1998)
33. Iwashita, K., Oda, M.: Micro-deformation mechanism of shear banding process based on modified distinct element method. Powder Technol. **109**(1), 192–205 (2000)
34. Jefferies, M.G.: Nor-Sand: a simple critical state model for sand. Geotechnique **43**(1), 91–103 (1993)
35. Jiang, M.J., Yu, H.-S., Harris, D.: A novel discrete model for granular material incorporating rolling resistance. Comput. Geotech. **32**(5), 340–357 (2005)
36. Kuhn, M.R., Bagi, K.: Specimen size effect in discrete element simulations of granular assemblies. J. Eng. Mech. **109**(1), 485–492 (2018)
37. Lade, P.V.: Static instability and liquefaction of loose fine sandy slopes. J Geotech. Eng.-Asce. **118**(1), 51–71 (1992)
38. Lade, P.V., Ibsen, L.B.: A study of the phase transformation and characteristic lines of sand. In: Deformation and Progressive Failure in Geomechanics IS-NAGOYA, pp. 353–358 (1997)
39. Lashkari, A., Khodadadi, M., Binesh, S.M., Rahman, Md.M.: Instability of particulate assemblies under constant shear drained stress path: DEM approach. Int. J. Geomech. **19**(6), 04019049 (2019)
40. Lee, K.L., Seed, H.B.: Dynamic strength of anisotropically consolidated sand. Proc. ASCE **93**(SM5), 169–190 (1967)
41. Li, X., Dafalias, Y.: Anisotropic critical state theory: role of fabric. J. Eng. Mech. **138**(3), 263–275 (2012)
42. Li, X.S.: A sand model with state-dependent dilatancy. Geotechnique **52**(3), 173–186 (2002)
43. Li, X.S., Dafalias, Y.F.: Dilatancy for cohesionless soils. Geotechnique **50**(4), 449–460 (2000)
44. Li, X.S., Dafalias, Y.F.: A constitutive framework for anisotropic sand including nonproportional loading. Geotechnique **54**(1), 41–55 (2004)
45. Li, X.S., Dafalias, Y.F., Wang, Z.-L.: State-dependant dilatancy in critical-state constitutive modelling of sand. Can. Geotech. J. **36**(4), 599–611 (1999)
46. Liu, Y., Liu, H., Mao, H.: The influence of rolling resistance on the stress-dilatancy and fabric anisotropy of granular materials. Granular Matter **20**(1), 1–16 (2018)
47. Lopera Perez, J.C., Kwok, C.Y., O'Sullivan, C., Huang, X., Hanley, K.J.: Assessing the quasi-static conditions for shearing in granular media within the critical state soil mechanics framework. Soils Found. **56**(1), 152–159 (2016)
48. Manzari, M.T., Dafalias, Y.F.: A critical state two-surface plasticity model for sands. Geotechnique **47**(2), 255–272 (1997)
49. Marketos, G., Bolton, M.D.: Flat boundaries and their effect on sand testing. Int. J. Numer. Anal. Meth. Geomech. **34**(8), 821–837 (2010)
50. MiDi, G.D.R.: On dense granular flows. Eur. Phys. J. E **14**(4), 341–365 (2004)
51. Minh, N., Cheng, Y.: A DEM investigation of the effect of particle-size distribution on one-dimensional compression. Geotechnique **63**(1), 44–53 (2013)
52. Minh, N., Cheng, Y., Thornton, C.: Strong force networks in granular mixtures. Granular Matter **16**(1), 69–78 (2014)
53. Mizanur, R.M., Lo, S.R.: Predicting the onset of static liquefaction of loose sand with fines. J. Geotech. Geoenviron. Eng. **138**(8), 1037–1041 (2012)
54. Mohamed, A., Gutierrez, M.: Comprehensive study of the effects of rolling resistance on the stress-strain and strain localization behavior of granular materials. Granular Matter **12**(5), 527–541 (2010)
55. Murthy, T.G., Loukidis, D., Carraro, J.A.H., Prezzi, M., Salgado, R.: Undrained monotonic response of clean and silty sands. Geotechnique **57**(3), 273–288 (2007)

56. Nakata, Y., Hyodo, M., Murata, H., Yasufuku, N.: Flow deformation of sands subjected to principal stress rotation. Soils Found. **38**(2), 115–128 (1998)
57. Nguyen, H.B.K.: Critical State Behaviour of Granular Materials and Associated Micro-Mechanics: A DEM Study. University of South Australia, Adelaide (2017)
58. Nguyen, H.B.K., Rahman, M.M., Cameron, D.A., Fourie, A.B.: The effect of consolidation path on undrained behaviour of sand - A DEM approach. In: A. M. Fusao Oka, Ryosuke Uzuoka, Sayuri Kimoto (eds.) Computer Methods and Recent Advances in Geomechanics. CRC Press: Taylor & Francis Group, pp. 175–180 (2015)
59. Nguyen, H.B.K., Rahman, M.M., Fourie, A.B.: Undrained behaviour of granular material and the role of fabric in isotropic and K0 consolidations: DEM approach. Geotechnique **67**(2), 153–167 (2017)
60. Nguyen, H.B.K., Rahman, M.M., Fourie, A.B.: Characteristic behavior of drained and undrained triaxial compression tests: DEM study. J. Geotech. Geoenviron. Eng. **144**(9), 1–13 (2018)
61. Nguyen, H.B.K., Rahman, M.M., Fourie, A.B.: How particle shape affects the critical state, triggering of instability and dilatancy of granular materials – results from a DEM study. Géotechnique (2020). https://doi.org/10.1680/jgeot.18.P.211
62. Nguyen, H.B.K., Rahman, M.M., Fourie, A.B.: Effect of Particle Shape on Constitutive Relation: DEM Study. J. Geotech. Geoenviron. Eng. **146**(7), 04020058 (2020)
63. O'sullivan, C., Wadee, M.A., Hanley, K.J., Barreto, D.: Use of DEM and elastic stability analysis to explain the influence of the intermediate principal stress on shear strength. Geotechnique, 1298–1309 (2013)
64. Oda, M.: Fabric tensor for discontinuous geological materials. Soils Found. **22**(4), 96–108 (1982)
65. Oda, M., Kazama, M.: Microstructure of shear bands and its relation to the mechanisms of dilatancy and failure of dense granular soils. Geotechnique **48**(4), 465–481 (1998)
66. Oda, M., Konishi, J., Nemat-Nasser, S.: Experimental micromechanical evaluation of strength of granular materials: effect of particle rolling. Mech. Mater. **1**, 269–283 (1982)
67. Perez, J.C.L., Kwok, C.Y., O'Sullivan, C., Huang, X., Hanley, K.J.: Exploring the micro-mechanics of triaxial instability in granular materials. Geotechnique, 1–16 (2016)
68. Plassiard, J., Belheine, N., Donzé, F.: A spherical discrete element model: calibration procedure and incremental response. Granular Matter **11**(5), 293–306 (2009)
69. Qadimi, A., Coop, M.R.: The undrained cyclic behaviour of a carbonate sand. Geotechnique **57**(9), 739–750 (2007)
70. Rabbi, A.T.M.Z., Rahman, M.M., Cameron, D.A.: Undrained behavior of silty sand and the role of isotropic and K0 consolidation. J. Geotech. Geoenviron. Eng. **144**(4), 1–11 (2018)
71. Rabbi, A.T.M.Z., Rahman, M.M., Cameron, D.A.: Critical state study of natural silty sand instability under undrained and constant shear drained path. Int. J. Geomech. **19**(8), 04019083 (2019)
72. Radjai, F., Wolf, D.E., Jean, M., Moreau, J.: Bimodal character of stress transmission in granular packings. Phys. Rev. Lett. **80**(1), 61–64 (1998)
73. Rahman, M., Baki, M., Lo, S.: Prediction of undrained monotonic and cyclic liquefaction behavior of sand with fines based on the equivalent granular state parameter. Int. J. Geomech. **14**(2), 254–266 (2014)
74. Rahman, M.M., Lo, S.-C.R., Dafalias, Y.F.: Modelling the static liquefaction of sand with low-plasticity fines. Geotechnique **64**(11), 881–894 (2014)
75. Rahman, M.M., Lo, S.R.: Undrained behaviour of sand-fines mixtures and their state parameters. J. Geotech. Geoenviron. Eng. **140**(7) (2014)
76. Rahman, M.M., Nguyen, H.B.K., Rabbi, A.T.M.Z.: The effect of consolidation on undrained behaviour of granular materials: experiment and DEM simulation. Geotech. Res. **5**(4), 199–217 (2018). https://doi.org/10.1680/jgere.17.00019
77. Rahman, M.M., Nguyen, H.B.K., Fourie, A.B., Kuhn, M.: Critical state soil mechanics for cyclic liquefaction and post-liquefaction behaviour: a DEM study. J. Geotech. Geoenviron. Eng. (2020). https://doi.org/10.1061/(ASCE)GT.1943-5606.0002453
78. Rothenburg, L., Bathurst, R.J.: Analytical study of induced anisotropy in idealized granular materials. Geotechnique **39**(4), 601–614 (1989)
79. Rowe, P.W.: The stress-dilatancy relation for static equilibrium of an assembly of particles in contact. Proc. R. Soc. Lond. Ser. A Math. Phys. Sci., **269**(1339), 500–527 (1962)
80. Satake, M.: Fabric tensor in granular materials. In: Proceedings of the IUTAM Symposium on Deformations and Failure of Granular Materials, pp. 93–96 (1982)
81. Sitharam, T.G., Vinod, J.S., Ravishankar, B.V.: Evaluation of undrained response from drained triaxial shear tests: DEM simulations and experiments. Geotechnique **58**(7), 605–608 (2008)
82. Sladen, J.A., D'Hollander, R.D., Krahn, J.: The liquefaction of sands, a collapse surface approach. Can. Geotech. J. **22**(4), 564–578 (1985)
83. Sukumaran, B., Leonards, G.A., Fox, J.P.: Discussion: liquefaction and postliquefaction behaviour of sand. J. Geotech. Geoenviron. Eng. **122**(6), 502–503 (1996)
84. Tang, H., Dong, Y., Chu, X., Zhang, X.: The influence of particle rolling and imperfections on the formation of shear bands in granular material. Granular Matter **18**(1), 1–12 (2016)
85. Vaid, Y.P., Sivathayalan, S., Stedman, D.: Influence of specimen-reconstituting method on the undrained response of sand. Geotech. Test. J. **22**(3), 187–195 (1999)
86. Yan, W., Dong, J.: Effect of particle grading on the response of an idealized granular assemblage. Int. J. Geomech. **11**(4), 276–285 (2011)
87. Yang, J.: Non-uniqueness of flow liquefaction line for loose sand. Geotechnique **52**(10), 757–760 (2002)
88. Yang, J., Dai, B.B.: Is the quasi-steady state a real behaviour? A micromechanical perspective. Geotechnique **61**(2), 175–183 (2011)
89. Yang, Z.X., Li, X.S., Yang, J.: Quantifying and modelling fabric anisotropy of granular soils. Geotechnique **58**(4), 237–248 (2008)
90. Yoshimine, M., Ishihara, K.: Flow potential of sand during liquefaction. Soils Found. **38**(3), 189–198 (1998)
91. Yoshimine, M., Ishihara, K., Vargas, W.: Effects of principal stress direction and intermediate principal stress on undrained shear behaviour of sand. Soils Found. **38**(3), 179–188 (1998)
92. Zhang, J., Lo, S.C.R., Rahman, M.M., Yan, J.: "Characterizing monotonic behaviour of pond ash within critical state approach. J. Geotech. Geoenviron. Eng., **144**(1) (2018)
93. Zhao, J., Guo, N.: Unique critical state characteristics in granular media considering fabric anisotropy. Geotechnique, 695–704 (2013)
94. Zhao, J., Guo, N.: Rotational resistance and shear-induced anisotropy in granular media. Acta Mech. Solida Sin. **27**(1), 1–14 (2014)
95. Zhao, S., Evans, T.M., Zhou, X.: Shear-induced anisotropy of granular materials with rolling resistance and particle shape effects. Int. J. Solids Struct. **150**, 268–281 (2018)
96. Zhou, W., Liu, J., Ma, G., Chang, X.: Three-dimensional DEM investigation of critical state and dilatancy behaviors of granular materials. Acta Geotech. **12**(3), 527–540 (2017)

97. Zhou, W., Xu, K., Ma, G., Yang, L., Chang, X.: Effects of particle size ratio on the macro- and microscopic behaviors of binary mixtures at the maximum packing efficiency state. Granular Matter **18**(4), 1–13 (2016)
98. Zhou, Y.C., Wright, B.D., Yang, R.Y., Xu, B.H., Yu, A.B.: Rolling friction in the dynamic simulation of sandpile formation. Physica Stat. Mech. Appl. **269**(2), 536–553 (1999)
99. Zhou, Y.C., Xu, B.H., Yu, A.B., Zulli, P.: Numerical investigation of the angle of repose of monosized spheres. Phys. Rev. E **64**, 213011 (2001)
100. Zhu, Y., Nie, Z., Gong, J.: Influence of the rolling-resistance-based shape of coarse particles on the shear responses of granular mixtures. Particuology (2020)